



**CHALMERS**  
UNIVERSITY OF TECHNOLOGY

## **Effect of the Preparation Methods on the Physicochemical Properties of Indium-Based Catalysts and Their Catalytic Performance for**

Downloaded from: <https://research.chalmers.se>, 2026-04-03 06:23 UTC

Citation for the original published paper (version of record):

Ho, H., Tizzanini, G., Ghosh, S. et al (2024). Effect of the Preparation Methods on the Physicochemical Properties of Indium-Based Catalysts and Their Catalytic Performance for CO<sub>2</sub> Hydrogenation to Methanol. *Energy & Fuels*, 38(6): 5407-5420. <http://dx.doi.org/10.1021/acs.energyfuels.3c04721>

N.B. When citing this work, cite the original published paper.

# Effect of the Preparation Methods on the Physicochemical Properties of Indium-Based Catalysts and Their Catalytic Performance for CO<sub>2</sub> Hydrogenation to Methanol

Published as part of *Energy & Fuels* virtual special issue “Recent Advances in CO<sub>2</sub> Conversion to Chemicals and Fuels”.

Phuoc Hoang Ho, Giovanni Tizzanini, Sreetama Ghosh, Wei Di, Jieling Shao, Oleg Pajalic, Lars Josefsson, Patricia Benito,\* Derek Creaser, and Louise Olsson\*



Cite This: <https://doi.org/10.1021/acs.energyfuels.3c04721>



Read Online

ACCESS |



Metrics & More

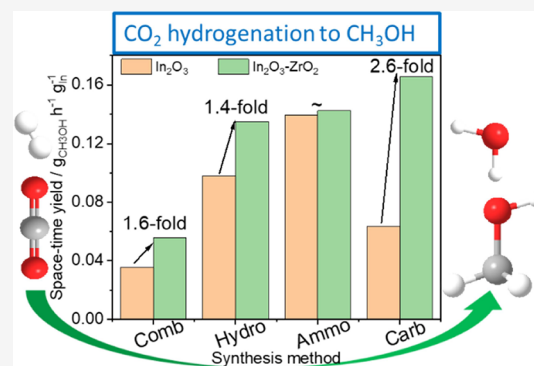


Article Recommendations



Supporting Information

**ABSTRACT:** Indium oxides (In<sub>2</sub>O<sub>3</sub>) and indium oxides supported zirconia (ZrO<sub>2</sub>) have been known possible alternatives for conventional copper-based catalysts in the CO<sub>2</sub>-hydrogenation to methanol. This study aims to investigate the effect of preparation techniques on the physicochemical properties of indium-based materials and their catalytic performance for the hydrogenation of CO<sub>2</sub> to methanol. Two series of both single oxide In<sub>2</sub>O<sub>3</sub> and binary In<sub>2</sub>O<sub>3</sub>-ZrO<sub>2</sub> have been synthesized by combustion, urea hydrolysis, and precipitation with different precipitating agents (sodium carbonate and ammonia/ethanol solution). Physicochemical properties of materials are characterized by elemental analysis, XRD, N<sub>2</sub> physisorption, SEM/EDX, micro-Raman, XPS, H<sub>2</sub>-TPR, and CO<sub>2</sub>-TPD. Cubic In<sub>2</sub>O<sub>3</sub> was the common phase generated by all four synthesis methods, except for urea hydrolysis, where rhombohedral In<sub>2</sub>O<sub>3</sub> was additionally present. The combustion method produced the materials with the lowest specific surface areas while the precipitation using ammonia/ethanol aided in creating more oxygen defects. The synthesis methods strongly influenced the degree of interaction between the oxides and resulted in improvements in properties that boosted the catalytic performance of the binary oxides compared to their single-oxide counterparts.



## 1. INTRODUCTION

Hydrogenation of carbon dioxide into methanol ( $\text{CO}_2 + 3\text{H}_2 \rightleftharpoons \text{CH}_3\text{OH} + \text{H}_2\text{O}$ ,  $\Delta H^\circ = -49.4 \text{ kJ mol}^{-1}$ ) is one of the interesting processes for the chemical valorization of CO<sub>2</sub> in which a greenhouse gas is transformed into a value-added product.<sup>1</sup> In this process, the methanol product can be further transformed into dimethyl ether, olefins (methanol to olefins, MTO), or gasoline (methanol to gasoline, MTG). Apart from a direct hydrogenation of CO<sub>2</sub> to methanol via the formate intermediate mechanism, the most competitive reaction is the reverse water gas shift ( $\text{CO}_2 + \text{H}_2 \rightleftharpoons \text{CO} + \text{H}_2\text{O}$ ) which creates CO. This CO intermediate can be further transformed into hydrocarbons via Fischer–Tropsch synthesis as well as oxygenates. As a result, the hydrogenation of CO<sub>2</sub> can produce various products including methanol, carbon monoxide (CO), oxygenates (e.g., dimethyl ether (DME)), and hydrocarbons (HCs).<sup>2</sup> Therefore, developing efficient selective catalysts plays an important role in the production of a target product.

The selection of hydrogenation of CO<sub>2</sub> to methanol is interesting because methanol can be used directly as a solvent or reactant for other industrial chemical production such as

formaldehyde, methyl methacrylate, acetic acid, methyl *tert*-butyl ether (MTBE), gasoline blending, and so on.<sup>3</sup> Especially, the use of methanol for sustainable aviation fuels (SAF) production becomes more attractive recently since European Union has recently targeted that 70% of jet fuels at EU airports will have to be green by 2050.<sup>4</sup> There are two directions of methanol conversion to SAF, namely, two-step and one-step (direct) process. For the two-step synthesis, methanol is initially converted into olefins via the MTO process (a combination of reverse water gas shift reaction and Fischer–Tropsch synthesis), and then, the olefin intermediates further oligomerized under conditions that produce olefins in the jet fuel range (C<sub>8</sub>–C<sub>16</sub>). A part of methanol is converted to DME,

Received: November 28, 2023

Revised: February 11, 2024

Accepted: February 12, 2024

which is then transformed over a catalyst to form jet fuel-range hydrocarbons and aromatics.<sup>5</sup> The direct hydrogenation of CO<sub>2</sub> (one step) to long-chain olefins (C<sub>8</sub>–C<sub>16</sub>) is a hot research topic and more challenging due to a quick deactivation of the catalysts by coke formation.<sup>6</sup> However, with an urgent need for SAF production, the production of SAF from CO<sub>2</sub> via methanol production has gained more attention because this process can take advantage of knowledge of MTO and methanol production. In this project, we focused on the first step, namely, the conversion of CO<sub>2</sub> to methanol. Finding a long-term stable catalyst for CO<sub>2</sub> hydrogenation to methanol is still challenging.

In 2013, using DFT calculation, Ye and co-workers found that In<sub>2</sub>O<sub>3</sub> would be a potential catalyst for CO<sub>2</sub> hydrogenation to methanol because it can suppress the reverse water gas shift reaction (RWGS) and subsequently increase the selectivity for methanol.<sup>7</sup> The prediction was quickly supported by experimental data in 2015.<sup>8</sup> In 2016, Martin et al. confirmed again the activity of bulk In<sub>2</sub>O<sub>3</sub>, and they also found that ZrO<sub>2</sub> was the best support for indium-based catalysts among the eight materials investigated (ZrO<sub>2</sub>, TiO<sub>2</sub>, ZnO, SiO<sub>2</sub>, Al<sub>2</sub>O<sub>3</sub>, activated carbon, SnO<sub>2</sub>, and MgO).<sup>9</sup> After that, indium-based catalysts have been extensively investigated with a focus on the effect of the promoters and the supports.<sup>10</sup> Indium oxide has a unique characteristic for the activation of both CO<sub>2</sub> and H<sub>2</sub>. It has been proposed that under the reaction conditions, hydrogen is first attracted by the surface oxygen and partially reduces the surface of indium oxide, resulting in the formation of under-coordinated indium sites (In<sub>2</sub>O<sub>3-x</sub>) and thus creating oxygen vacancies that attract the insertion of CO<sub>2</sub> (CO<sub>2</sub> activation).<sup>7</sup> After the reaction, the former vacancy site remains filled by an oxygen atom. The recreation of vacancy can be done by the dissociation of hydrogen to form In–H and adjacent In–OH. The elimination of H<sub>2</sub>O via hydride transfer from In–H to the –OH group aids in restoring the vacancy.<sup>11</sup>

There are two stable phases of In<sub>2</sub>O<sub>3</sub> reported in the literature, namely, body-centered cubic (bcc-, *Ia*3, *a* = 10.118 Å) and rhombohedral (rh-, *R*3c, *a* = 5.478 and *c* = 14.51 Å)<sup>12</sup> and the former is the more common structure than the latter. For bare In<sub>2</sub>O<sub>3</sub> catalysts, the crystal structure of In<sub>2</sub>O<sub>3</sub> influenced the methanol productivity. Shi et al. have recently reported that the rhombohedral (hexagonal as ascribed by the authors) In<sub>2</sub>O<sub>3</sub> was more active than cubic In<sub>2</sub>O<sub>3</sub> (space-time yield of methanol around 2.35 versus 2.0 mmol g<sub>cat</sub><sup>-1</sup> h<sup>-1</sup>) and especially the mixed phase exhibited even better performance than the single phase. The authors correlated better activity with improved textural properties, more oxygen vacancy content, and higher strength and adsorption capacity of CO<sub>2</sub>.<sup>13</sup> In contrast, in another work, Yang and co-workers found that although the rhombohedral In<sub>2</sub>O<sub>3</sub> had higher methanol selectivity than cubic In<sub>2</sub>O<sub>3</sub>, it showed lower methanol productivity (space-time yield of methanol around 1.8 versus 3.0 mmol g<sub>cat</sub><sup>-1</sup> h<sup>-1</sup>). The discrepancy between the two studies could be related to the preparation method of the catalysts. For the mechanism, it has been proposed that CO<sub>2</sub> hydrogenation to methanol over In<sub>2</sub>O<sub>3</sub> follows the formate pathway.<sup>13</sup>

The supported In<sub>2</sub>O<sub>3</sub> with ZrO<sub>2</sub> showed significant improvement in methanol productivity compared to the bare In<sub>2</sub>O<sub>3</sub> by boosting the generation of oxygen vacancies, and, in this regard, monoclinic ZrO<sub>2</sub> was superior to its tetragonal phase.<sup>14</sup> Moreover, ZrO<sub>2</sub> can also aid in suppressing the over-reduction of In<sub>2</sub>O<sub>3</sub> by the optimization of surface oxygen

vacancy of In<sub>2</sub>O<sub>3</sub>.<sup>15</sup> Tsoukalou et al. confirmed that the In<sub>2</sub>O<sub>3</sub>/m-ZrO<sub>2</sub> showed not only the highest productivity of methanol but also the most stable activity with time-on-stream.<sup>16</sup> With the support of a powerful technique, operando X-ray absorption spectroscopy, the authors highlighted that in the In<sub>2</sub>O<sub>3</sub>/m-ZrO<sub>2</sub> catalyst, the solid solution m-ZrO<sub>2</sub>:In prevents the over-reduction of In<sup>3+</sup> to In<sup>0</sup> and subsequently against the deactivation of this catalyst. With in situ Raman and quasi-in situ XPS, Yang and co-workers demonstrated that a high dispersion of In–O–In together with the improved electron density of In<sub>2</sub>O<sub>3</sub> can promote the dissociation of H<sub>2</sub> and hydrogenation of the formate intermediate to methanol.<sup>17</sup> ZrO<sub>2</sub> plays an important role in the stabilization of the formate intermediate,<sup>18</sup> where the bonding strength between the intermediate and Zr sites should be at a modest degree to boost the hydrogenation of the formate intermediate (producing CH<sub>3</sub>OH) rather than the C–O bond cleavage of HCOO\* (forming CO).<sup>19</sup>

Because the methanol productivity from CO<sub>2</sub> hydrogenation is strongly influenced by the structure of both the In<sub>2</sub>O<sub>3</sub> active phase and ZrO<sub>2</sub> support, the preparation method is expected to have an important role in the development of the catalysts. Yanling and co-workers have recently reported a significant effect of the preparation method for CO<sub>2</sub> hydrogenation to methanol over binary oxides of In<sub>2</sub>O<sub>3</sub> and ZrO<sub>2</sub> using four different methods (coprecipitation, precipitation-deposition, ball milling, and incipient wetness impregnation).<sup>20</sup> In the present work, we aim to further complete the puzzle by illustrating the effect of the preparation method on the methanol productivity from CO<sub>2</sub> hydrogenation over first the single oxide and how catalytic performance further changes by interactions with ZrO<sub>2</sub>. Two series of single oxide In<sub>2</sub>O<sub>3</sub> and binary oxide In<sub>2</sub>O<sub>3</sub>–ZrO<sub>2</sub> were prepared using various methods including urea combustion, urea hydrolysis, and precipitation/coprecipitation using different agents (ammonia solution and sodium carbonate). The physicochemical properties of these materials were characterized with various techniques such as elemental analysis, X-ray diffraction (XRD), N<sub>2</sub> physisorption, scanning electronic microscopy (SEM), micro-Raman, CO chemisorption, temperature-programmed reduction with H<sub>2</sub> (H<sub>2</sub>-TPR), temperature-programmed desorption of CO<sub>2</sub> (CO<sub>2</sub>-TPD), diffuse reflectance infrared Fourier transform spectroscopy (DRIFTS), and X-ray photon spectroscopy (XPS). The catalytic performance of CO<sub>2</sub> hydrogenation to methanol was investigated using a fixed-bed reactor at 4 MPa.

## 2. EXPERIMENTAL SECTION

**2.1. Chemicals.** In(NO<sub>3</sub>)<sub>3</sub>·xH<sub>2</sub>O (≥99.99%, Alfa Aesar), ZrO(NO<sub>3</sub>)<sub>2</sub>·yH<sub>2</sub>O (≥99%, Sigma-Aldrich), NH<sub>4</sub>OH solution (25%, VWR Chemical), urea (≥99.5%, Sigma-Aldrich), and Na<sub>2</sub>CO<sub>3</sub> (≥99.5%, Sigma-Aldrich) were used for the catalyst synthesis. Thermogravimetric analysis (TGA) was used to determine the water content in the In(NO<sub>3</sub>)<sub>3</sub>·xH<sub>2</sub>O and ZrO(NO<sub>3</sub>)<sub>2</sub>·yH<sub>2</sub>O precursors (Figure S1). The weight loss at 800 °C was 38.7 and 36.4% for the former and the latter, respectively. With the assumption that the product at 800 °C was the pure oxide of In<sub>2</sub>O<sub>3</sub> and ZrO<sub>2</sub>, the values for *x* and *y* were found to be 3.2 and 6.0, respectively.

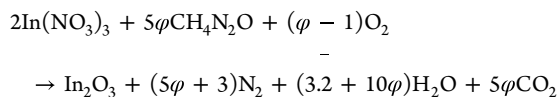
**2.2. Catalyst Preparation.** The synthesis protocols were designed to obtain about 4 g of each catalyst containing solely In<sub>2</sub>O<sub>3</sub> and mixed oxides of In<sub>2</sub>O<sub>3</sub>–ZrO<sub>2</sub> (molar ratio 1:1). Three synthesis methods were used including urea combustion, urea hydrolysis, and (co)precipitation with NH<sub>4</sub>OH and Na<sub>2</sub>CO<sub>3</sub>.

A total of 8 samples were synthesized, and their acronym names, theoretical compositions, and preparation methods are shown in Table 1.

**Table 1. Information on Labels, Theoretical Compositions, and the Preparation Methods of the Catalysts**

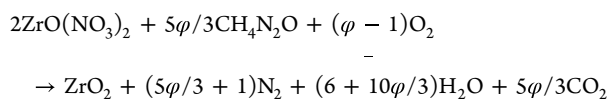
acronym name	composition	preparation method
I-comb	In <sub>2</sub> O <sub>3</sub>	urea combustion
I-ammo	In <sub>2</sub> O <sub>3</sub>	NH <sub>4</sub> /EtOH precipitation
I-hydro	In <sub>2</sub> O <sub>3</sub>	urea hydrolysis
I-carb	In <sub>2</sub> O <sub>3</sub>	Na <sub>2</sub> CO <sub>3</sub> precipitation
IZ-comb	In <sub>2</sub> O <sub>3</sub> -ZrO <sub>2</sub>	urea combustion
IZ-ammo	In <sub>2</sub> O <sub>3</sub> -ZrO <sub>2</sub>	NH <sub>4</sub> OH/ethanol precipitation
IZ-hydro	In <sub>2</sub> O <sub>3</sub> -ZrO <sub>2</sub>	urea hydrolysis
IZ-carb	In <sub>2</sub> O <sub>3</sub> -ZrO <sub>2</sub>	Na <sub>2</sub> CO <sub>3</sub> precipitation

**2.2.1. Combustion with Urea.** In the pure In<sub>2</sub>O<sub>3</sub> catalyst synthesis, 10.23 g of In(NO<sub>3</sub>)<sub>3</sub>·xH<sub>2</sub>O and 8.65 g of urea were mixed with a minimum amount of Milli-Q water in a ceramic crucible and kept under stirring for 1 h. The ratio between urea and indium nitrate precursor corresponded to the fuel-to-oxidizer ratio ( $\varphi$ ) of 2, according to the reaction stoichiometry:



After that, the crucible was transferred into an oven and heated from 20 to 500 °C (ramp of 5 °C min<sup>-1</sup>) and held at 500 °C for 6 h. This synthesis yielded a yellowish In<sub>2</sub>O<sub>3</sub> product in the form of a light, fragile, and foamy solid (Figure S2). The catalyst was denoted as I-comb, where “I” stands for In<sub>2</sub>O<sub>3</sub> and “comb” represents the combustion method.

The mixed oxide In<sub>2</sub>O<sub>3</sub>-ZrO<sub>2</sub> was synthesized with the same protocol using 7.08 g of In(NO<sub>3</sub>)<sub>3</sub>·xH<sub>2</sub>O, 3.39 g of ZrO(NO<sub>3</sub>)<sub>2</sub>·yH<sub>2</sub>O, and 7.99 g of urea. Now, in addition to the In(NO<sub>3</sub>)<sub>3</sub> combustion shown above, the ZrO(NO<sub>3</sub>)<sub>2</sub> combustion occurred with stoichiometry:



The catalyst was denoted as IZ-comb, where “IZ” stands for In<sub>2</sub>O<sub>3</sub>-ZrO<sub>2</sub>.

**2.2.2. Urea Hydrolysis.** In a typical synthesis, 10.23 g In(NO<sub>3</sub>)<sub>3</sub>·xH<sub>2</sub>O and 25.96 g of urea were mixed with 150 mL of Milli-Q water in a round-bottom flask and kept under stirring for 30 min. The flask was connected to a reflux system and it was heated to 90 °C and kept for 16 h. The milky suspension was centrifugated and washed several times with a total of 1 L of distilled water. The solid product was dried at 80 °C for 16 h and subsequently calcined at 500 °C for 6 h (heating rate 5 °C min<sup>-1</sup>). The catalyst was denoted as I-hydro, where “hydro” stands for the urea hydrolysis method.

A mixed oxide of the In<sub>2</sub>O<sub>3</sub>-ZrO<sub>2</sub> catalyst was prepared with a similar protocol using 7.08 g of In(NO<sub>3</sub>)<sub>3</sub>·xH<sub>2</sub>O, 3.39 g of ZrO(NO<sub>3</sub>)<sub>2</sub>·yH<sub>2</sub>O, and 29.97 g of urea. This catalyst was denoted as IZ-hydro.

**2.2.3. Precipitation Using NH<sub>4</sub>OH and Ethanol.** In a typical synthesis, 10.23 g precursor of indium was dissolved in 150 mL of Milli-Q water in a beaker and the solution was kept stirring for 30 min. Thereafter, a mixture of NH<sub>4</sub>OH solution (25% in water) and absolute ethanol (volume ratio 1:2) was added dropwise into the In(NO<sub>3</sub>)<sub>3</sub> solution until the pH reached around 9.2. The milky solution was kept under stirring for 30 min and then it was aged at 80 °C for another 30 min. Finally, the solution was centrifugated and washed with 1 L of Milli-Q H<sub>2</sub>O. The solid product was dried at 80 °C for 16 h and subsequently calcined at 500 °C for 6 h (5 °C min<sup>-1</sup>).

The catalyst was denoted as I-ammo, where “ammo” stands for the employment of an ammonia solution.

A mixed oxide of In<sub>2</sub>O<sub>3</sub>-ZrO<sub>2</sub> was synthesized in a similar protocol using 7.08 g of In(NO<sub>3</sub>)<sub>3</sub>·xH<sub>2</sub>O and 3.39 g of ZrO(NO<sub>3</sub>)<sub>2</sub>·yH<sub>2</sub>O. The catalyst was labeled as IZ-ammo.

**2.2.4. Precipitation Using Na<sub>2</sub>CO<sub>3</sub>.** One sample containing the mixed oxide of In<sub>2</sub>O<sub>3</sub>-ZrO<sub>2</sub> was prepared using 7.08 g of In(NO<sub>3</sub>)<sub>3</sub>·xH<sub>2</sub>O and 3.39 g of ZrO(NO<sub>3</sub>)<sub>2</sub>·yH<sub>2</sub>O. The same procedure as the NH<sub>4</sub>OH/EtOH precipitation was followed, however, a 1 M solution of Na<sub>2</sub>CO<sub>3</sub> was used as the precipitating agent to replace the mixed NH<sub>4</sub>OH/EtOH solution. The resulting precipitate was aged at 25 °C for 30 min. After that, the suspension was centrifugated and washed with 4 L of hot water (80 °C), until neutral pH, to remove Na as much as possible. The catalyst was labeled IZ-carb, where “carb” stands for the use of carbonate as a precipitating agent.

Single oxide of In<sub>2</sub>O<sub>3</sub> was synthesized using the same protocol but using a solution containing 10.23 g In(NO<sub>3</sub>)<sub>3</sub>·xH<sub>2</sub>O in 150 mL of Milli-Q water. The catalyst was denoted as I-carb.

**2.3. Characterization Techniques.** Thermogravimetric analysis (TGA) of In(NO<sub>3</sub>)<sub>3</sub>·xH<sub>2</sub>O and ZrO(NO<sub>3</sub>)<sub>2</sub>·yH<sub>2</sub>O were measured using a Mettler Toledo TGA/DSC 3+ instrument in air flow (ramp of 10 °C min<sup>-1</sup>).

Elemental compositions of the catalysts were analyzed using inductively coupled plasma sector field mass spectrometry (ICP-SFMS). The measurements were performed by ALS Scandinavia (Luleå, Sweden).

X-ray diffraction, X-ray photon spectroscopy, and nitrogen physisorption were analyzed to determine crystallite phase, oxidation states, and specific surface area, respectively. A description of these techniques can be found in our previous work.<sup>21</sup>

Scanning electron microscopy was used to investigate the morphology of the catalysts. High-resolution images were acquired using a JEOL JSM-7800F Prime instrument equipped with an EDX (energy-dispersive X-ray) detector. Raman spectra were recorded using Raman microscope alpha300 R, WITec with a laser source at  $\lambda = 532$  nm.

CO<sub>2</sub>-TPD measurements were performed using a calorimeter (Sensys DSC, SETARAM instrumentation) coupled with a mass spectrometer (HPR-20 QIC, Hidden analytical). The sieved catalyst (50 mg with a particle size of 180–250  $\mu\text{m}$ ) was loaded in a quartz fixed-bed tube (4 mm of inner diameter). The sample was pretreated in Ar (20 mL min<sup>-1</sup>) at 300 °C for 0.5 h and subsequently cooled to 25 °C. A flow of 5000 ppm of CO<sub>2</sub>/Ar (20 mL min<sup>-1</sup>) was introduced to the reactor for 1 h in the adsorption step. After that, the reactor was purged with Ar for 30 min to remove the weakly adsorbed CO<sub>2</sub>. Eventually, the reactor was subsequently heated from 25 to 700 °C (with a ramp of 10 °C min<sup>-1</sup>) and kept at 700 °C for 15 min in Ar flow. CO<sub>2</sub> was tracked by the mass number  $m/z = 44$ .

H<sub>2</sub>-TPR measurements were performed using the same instrument setup as CO<sub>2</sub>-TPD. Approximately 20 mg of the catalyst was pretreated under the same conditions as that of CO<sub>2</sub>-TPD. A flow of 1 vol % H<sub>2</sub>/Ar (20 mL min<sup>-1</sup>) was subsequently flown through the reactor at 25 °C for 0.5 h. The reactor was then heated from 25 to 800 °C (10 °C min<sup>-1</sup>) and held at 800 °C for 15 min in Ar flow. H<sub>2</sub> was tracked by the mass number  $m/z = 2$ .

Diffuse reflectance infrared Fourier transform spectroscopy (DRIFTS) spectra were carried out with a Vertex 70 spectrometer using a mercury-cadmium-telluride detector (MCT, cooled by liquid nitrogen). The sample (powder) was loaded into a cell (high-temperature reaction cell purchased from Harrick Praying Mantis). Detailed information on the instrument setup can be found elsewhere.<sup>21</sup> Prior to each experiment, the sample was heated at 400 °C in a pure Ar flow for 30 min and subsequently cooled to 35 °C and held at this temperature for 1 h. A background spectrum was recorded at 35 °C. After that, the sample was exposed to a flow of 2000 ppm of CO<sub>2</sub>/Ar for 90 min followed by a flow of pure Ar. The spectra were recorded (every minute) for 100 min as soon as CO<sub>2</sub> gas was flown over the sample. It meant that a total of 100 scans were recorded including 90 scans under CO<sub>2</sub> flow and 10 scans in Ar

(purging). The last spectrum (100<sup>th</sup> scan) of each sample was reported for comparison purposes.

**2.4. Catalytic Tests.** The catalytic test was performed in a fixed-bed tubular stainless-steel reactor (VINCI Technologies, France, inner diameter  $\times$  length = 1.27  $\times$  21.5 cm). The reactor's total volume was 12.1 cm<sup>3</sup> and it was vertically positioned, with a thermocouple attached to its bottom that ran up to contact with the catalyst bed. Catalysts (particle sizes of 250 and 500  $\mu$ m) were used for the activity tests to avoid an excessive pressure drop over the catalyst bed. For comparison purposes, the activity tests were designed by keeping the same amount of In metal (500 mg) in each test sample. This required 605 mg of In<sub>2</sub>O<sub>3</sub> and 873 mg of In<sub>2</sub>O<sub>3</sub>-ZrO<sub>2</sub>. The catalyst was diluted with SiC (the same particle size) so that the total mass of the catalytic bed was 1 g. In this way, all tests were performed with the same weight hourly space velocity (WHSV) of 6000 mL g<sub>catalyst</sub><sup>-1</sup> h<sup>-1</sup> (or 12,000 mL g<sub>in</sub><sup>-1</sup> h<sup>-1</sup>). After a leak test at 40 bar, the catalyst was heated at 350 °C for 1 h in Ar (150 mL min<sup>-1</sup>). The feed gas was then switched to a mixture of H<sub>2</sub> and CO<sub>2</sub> (molar ratio of CO<sub>2</sub>:H<sub>2</sub> = 1:3, a total flow of 100 mL min<sup>-1</sup>), and the reactor was pressurized to 40 bar. The catalytic tests were measured at five points of temperatures from 350 to 250 °C (interval step of 25 °C). Three measurements are taken for each temperature point with a total reaction time of approximately 75 min to ensure that the steady state is reached. Detailed information on the analytical method and gas chromatography instrument can be found in our previous study.<sup>22</sup>

The apparent activation energy ( $E_a$ ) of CO<sub>2</sub> on each catalyst was determined from the slope of the Arrhenius plot in which all points of temperatures were selected at a conversion of CO<sub>2</sub> lower than 20%.<sup>23</sup>

The criteria for the estimation of transport effects (mass and heat) were calculated based on the guideline described elsewhere for the best catalyst (IZ-carb).<sup>24</sup> Detailed calculations can be found in the Supporting Information. It was noted that under the highest conversion of CO<sub>2</sub> on the most active catalyst, the Weisz-Prater and Maers parameters were WP = 0.156 and MP = 0.008, respectively. Since WP < 0.6 and MP < 0.15, both intraparticle and interphase mass transfer limitations could be neglected.

### 3. RESULTS AND DISCUSSION

**3.1. Catalyst Characterization.** For each synthesis, the theoretical amount of the materials after calcination is approximately 4.0 g. The urea hydrolysis and coprecipitation (using either NH<sub>4</sub>OH or Na<sub>2</sub>CO<sub>3</sub>) methods provided approximately 3.7–3.9 g of product which corresponded to a yield of 93–98% for both single In<sub>2</sub>O<sub>3</sub> and mixed oxides. By contrast, the urea combustion method only produced approximately 2.2 g of the materials (55% yield). The elemental compositions of the mixed oxide catalysts determined by ICP-SFMS are shown in Table 2. For binary

**Table 2. Elemental Composition of the Catalysts**

catalyst	In/molar %	Zr/molar %	Na/ppm
IZ-comb	48.23	51.77	
IZ-hydro	66.11	33.89	
IZ-ammo	64.91	35.09	
IZ-carb	66.98	33.02	<50

In<sub>2</sub>O<sub>3</sub>-ZrO<sub>2</sub>, three samples of IZ-hydro, IZ-ammo, and IZ-carb have the molar ratio of In/Zr  $\approx$  1.85–2.03 which was very close to the theoretical value of 2.0. Notably, the In/Zr of the IZ-comb was only half of the theoretical value. A significant loss in yield of the I-comb and a low In/Zr of the IZ-comb sample were attributed to a loss of the In(NO<sub>3</sub>)<sub>3</sub> precursor during the combustion. A quick ignition of the combustion probably induced the evaporation of water carrying along with it some In(NO<sub>3</sub>)<sub>3</sub> precursor. The content of Na in the IZ-carb

was negligible, suggesting that Na<sub>2</sub>CO<sub>3</sub> was completely removed during the washing step.

Figure 1 presents the XRD patterns of In<sub>2</sub>O<sub>3</sub> and In<sub>2</sub>O<sub>3</sub>-ZrO<sub>2</sub> prepared by the different synthesis methods. The

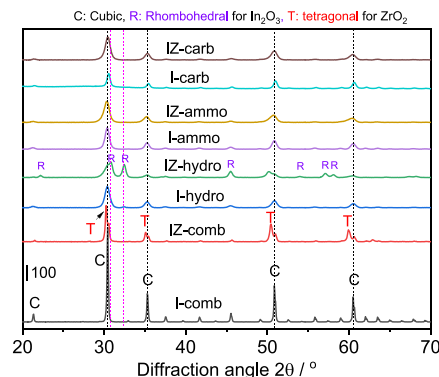


**Figure 1.** XRD patterns of In<sub>2</sub>O<sub>3</sub> and In<sub>2</sub>O<sub>3</sub>-ZrO<sub>2</sub> prepared by different methods.

reflections of a cubic structure (space group  $Ia\bar{3}$  (206), PDF 00-006-0146) were found for all samples of In<sub>2</sub>O<sub>3</sub> regardless of the synthesis method, which was in line with the literature.<sup>13</sup> However, the patterns of the In<sub>2</sub>O<sub>3</sub> sample prepared by urea hydrolysis showed also weak reflections at around  $2\theta$  of 32.5° and 45.6° which were characteristic reflections of the rhombohedral phase (PDF 04-001-8476).<sup>13,25,26</sup> This indicated that the urea hydrolysis method produced a trace of the side phase of the rhombohedral structure apart from the main cubic one. The crystal size of In<sub>2</sub>O<sub>3</sub> was calculated with Scherrer's equation using the input information on the plane (431) at  $2\theta$  of 45.5°. The result showed that the preparation method significantly influenced the crystallite sizes. The combustion method generated In<sub>2</sub>O<sub>3</sub> with a crystallite size of 39 nm (I-comb), which was approximately 3-fold larger than those prepared by other methods, for example, the urea hydrolysis (I-hydro, 12 nm) and precipitation with ammonia (I-ammo, 13 nm) or with Na<sub>2</sub>CO<sub>3</sub> (I-carb, 19 nm).

For In<sub>2</sub>O<sub>3</sub>-ZrO<sub>2</sub> catalysts, IZ-ammo and IZ-carb showed a solid solution of In<sub>2</sub>O<sub>3</sub> and ZrO<sub>2</sub> with a cubic structure (like Zr<sub>0.18</sub>In<sub>1.75</sub>O<sub>3</sub>, PDF 04-006-0768) (Figure 1a). This structure was also found in the IZ-hydro sample. However, apart from the cubic structure, the IZ-hydro catalyst also had a rhombohedral phase which was similar to the case of the I-hydro sample. By contrast, the pattern of the IZ-comb showed the reflections assigned to the cubic phase of In<sub>2</sub>O<sub>3</sub> as well as the tetragonal ZrO<sub>2</sub> (PDF 00-065-0729).<sup>14</sup> It should be noted that the interpretation of the phase for each In<sub>2</sub>O<sub>3</sub>-ZrO<sub>2</sub> catalyst was based on a comparison with its In<sub>2</sub>O<sub>3</sub> counterpart; however, the interference with the phase of ZrO<sub>2</sub> could not be excluded, especially in the case of the IZ-hydro sample in which the new phase of rhombohedral In<sub>2</sub>O<sub>3</sub> was identified. Therefore, four samples of ZrO<sub>2</sub> were prepared with similar methods as the In<sub>2</sub>O<sub>3</sub> counterparts, and their XRD patterns are presented in Figure S3. Both Z-hydro and Z-carb showed the same patterns of tetragonal ZrO<sub>2</sub> (PDF 00-065-0729) while Z-ammo and Z-comb exhibited complicated patterns assigned for both tetragonal and monoclinic ZrO<sub>2</sub>.<sup>20</sup> A comparison of the patterns of In<sub>2</sub>O<sub>3</sub>, ZrO<sub>2</sub>, and In<sub>2</sub>O<sub>3</sub>-ZrO<sub>2</sub> samples prepared with the same method was matched to clarify if the patterns of ZrO<sub>2</sub> phases would interfere with the interpretation of the

$\text{In}_2\text{O}_3$  phases (Figure S4). For the coprecipitation method using sodium carbonate and the urea hydrolysis, the pattern of tetragonal  $\text{ZrO}_2$  almost overlapped with the cubic  $\text{In}_2\text{O}_3$  (Figure S4b,d), and thus, the patterns of  $\text{In}_2\text{O}_3\text{-ZrO}_2$  have likely reassembled the patterns of their  $\text{In}_2\text{O}_3$  counterparts. In the case of the coprecipitation using ammonia solution, the IZ-ammo showed a very similar pattern with I-ammo, but not with Z-ammo (Figure S4a). The average cell parameter (cubic structure) calculated for two reflections at around  $2\theta$  of  $30.4^\circ$  and  $35.3^\circ$  is  $10.189 \pm 0.005$  and  $10.211 \pm 0.006$  Å, respectively. This suggests the formation of a solid solution between  $\text{In}_2\text{O}_3$  and  $\text{ZrO}_2$  in the IZ-ammo reassembled the structure of the I-ammo. For the combustion method, the reflections of the  $\text{ZrO}_2$  phase were identified in the pattern of the IZ-comb. The effect of the synthesis methods on the crystallite sizes of  $\text{In}_2\text{O}_3\text{-ZrO}_2$  catalysts was similar to  $\text{In}_2\text{O}_3$ . The IZ-comb showed a large crystallite size of 29 nm whereas the other samples had a size in the range of 12–16 nm. These particle sizes are similar to those we determined in an earlier study, where we analyzed  $\text{In}_2\text{O}_3$  prepared by the precipitation with  $\text{Na}_2\text{CO}_3$  using TEM, resulting in particle sizes around 12–16 nm.<sup>22</sup>

Figure 2 displays the SEM images of  $\text{In}_2\text{O}_3$  and  $\text{In}_2\text{O}_3\text{-ZrO}_2$  catalysts prepared by different methods. The I-comb showed an agglomeration of bent particles, around 200 nm long (Figure 2a). This morphology was also found in the IZ-comb

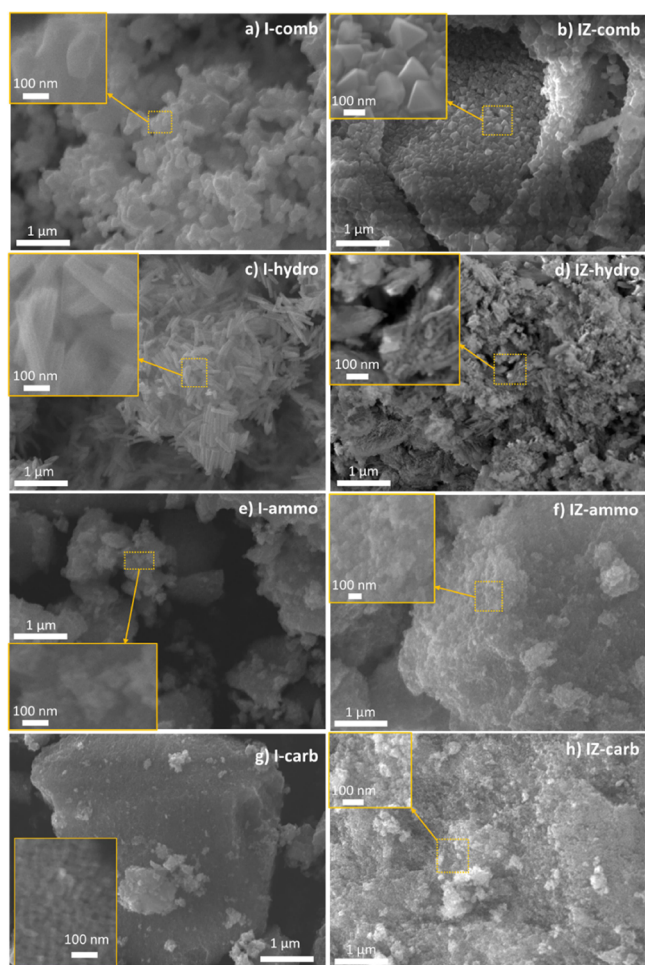


**Figure 2.** SEM images of  $\text{In}_2\text{O}_3$  and  $\text{In}_2\text{O}_3\text{-ZrO}_2$  catalysts prepared by different synthesis methods.

sample, together with well-defined tetragonal crystals (Figure 2b) which belonged to the tetragonal  $\text{ZrO}_2$ . This is consistent with the XRD data as both the cubic phase of  $\text{In}_2\text{O}_3$  and tetragonal  $\text{ZrO}_2$  were identified from the XRD patterns of the IZ-comb. The indium oxide prepared with the urea hydrolysis—I-hydro was composed of rod particles with a length of approximately 500 nm (Figure 2c) which agrees with the literature.<sup>27</sup> The rod morphology was also partially observed in the IZ-hydro, together with a cluster of ill-defined shapes (Figure 2d). Compared with the phase identified from XRD, it is hypothesized that the rod particles could be associated with the cubic structure of the solid solution of  $\text{In}_2\text{O}_3$  and  $\text{ZrO}_2$ , whereas the cluster morphology perhaps belonged to the hexagonal phase (rhombohedral). Both two samples of I-ammo and I-carb showed large clusters with a compact surface (Figure 2e,g). Their  $\text{In}_2\text{O}_3\text{-ZrO}_2$  counterparts, IZ-ammo and IZ-carb, also showed similar morphology; however, the clusters were smaller, and the surface was rougher than I-ammo and I-carb (Figure 2f,h).

More measurements with EDX elemental mapping were performed to examine the distribution of In and Zr elements in  $\text{In}_2\text{O}_3\text{-ZrO}_2$  samples and the results are shown in Figure 3. Overlapping signals of In, Zr, and O were found for the IZ-UH (Figure 3b–b(3)) and IZ-carb (Figure 3c–c(3)), suggesting a homogeneous distribution in the samples. For the IZ-comb sample, the element signals of In and Zr were also overlapping in most of the areas. However, it was noted that at least two areas were characteristics of indium-rich locations as guided by the circles in Figure 3a–a(2). To gain further information, the compositions of eight selected areas on each sample were analyzed by EDX with the point/area mode, and the data are presented in Figure S5. The data for the IZ-comb sample confirmed that there were two areas with indium-rich compositions with In/Zr molar ratios of 6.0–7.0 (points 7 and 8 in Figure S5) while the other 6 points had an average ratio of In/Zr of  $1.2 \pm 0.1$ . By contrast, the IZ-hydro and IZ-carb showed similar average ratios of In/Zr around 2.3. Considering that there is a variation in EDX mapping results due to the chosen areas, the In/Zr ratios derived from EDX measurements are consistent with the results of ICP measurements. It would be concluded that the combustion method does not control well the composition of the In and Zr compared to urea hydrolysis and coprecipitation counterparts.

To confirm the presence of different phases of  $\text{In}_2\text{O}_3$  in the catalysts, micro-Raman measurements were performed, and the results are presented in Figure 4. Five main frequency values of Raman active vibrations were observed in all the spectra at approximately 133 (In–O vibration of  $\text{InO}_6$  structure units,  $E_{2g}$ ), 308 (bending vibration  $\delta$  ( $\text{InO}_6$ ) of octahedrons,  $E_{1g}$ ), 369 (stretching vibrations of the In–O–In,  $E_{2g}$ ), 498 (stretching vibrations  $\nu$  ( $\text{InO}_6$ ) octahedrons,  $A_{1g}$ ), and  $631 \text{ cm}^{-1}$  ( $\nu$  ( $\text{InO}_6$ ),  $E_{2g}$ ), which are characteristic of the vibration modes of bcc- $\text{In}_2\text{O}_3$  ( $Ia3$ ).<sup>12,28</sup> Moreover, the vibration feature at  $369 \text{ cm}^{-1}$  also reflects the oxygen vacancies in the  $\text{In}_2\text{O}_3$  structure.<sup>29</sup> Therefore, a relative ratio of the intensity of this band (I2) and the band at  $308 \text{ cm}^{-1}$  (I1) is usually used to compare the oxygen vacancy density between the materials.<sup>28</sup> The ratio of I2/I1 was found to be around 0.91–0.96 and 0.71–0.78 for the  $\text{In}_2\text{O}_3\text{-ZrO}_2$  and  $\text{In}_2\text{O}_3$ , respectively (Table 3). This indicated that the presence of  $\text{ZrO}_2$  induced an increase in the number of oxygen vacancies compared to the bare  $\text{In}_2\text{O}_3$ . Especially, the Raman shift around  $165 \text{ cm}^{-1}$  was also observed for the I-hydro and IZ-

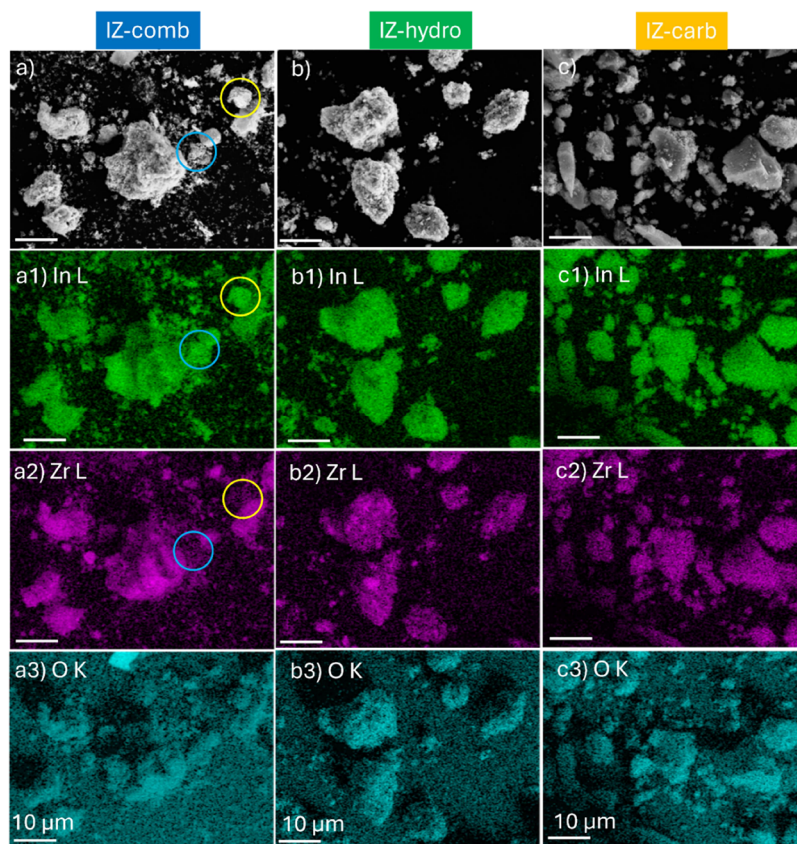


**Figure 3.** Selected elemental maps of three  $\text{In}_2\text{O}_3\text{-ZrO}_2$  samples from SEM/EDX analysis (IZ-com: a–a3; IZ-hydro: b–b3; and IZ-carb: c–c3): electron images a–c were taken at magnification of 3000. The bar scale in all figures is  $10\ \mu\text{m}$ . Maps of In (L): a1, b1, and c1; maps of Zr (L): a2, b2, and c2; and maps of O (K): a3, b3, and c3. The circles in figure a, a1 and a2 mark the indium-rich areas (more detailed information is presented in Figure S6).

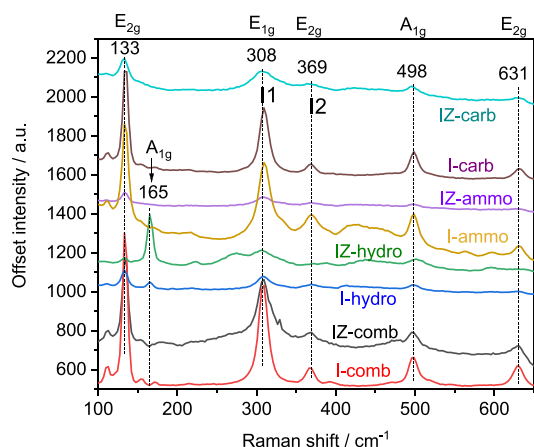


**Figure 4.** Raman spectra of  $\text{In}_2\text{O}_3$  and  $\text{In}_2\text{O}_3\text{-ZrO}_2$  catalysts prepared with different methods.

hydro samples. This band is characteristic of the rhombohedral structure which was consistent with the XRD data.<sup>25</sup>

Figures S6 and S7 present the  $\text{N}_2$ -physisorption isotherms of the different catalysts. The isotherms of the two combustion samples (I-comb and IZ-comb) were matched with type II according to the IUPAC classification,<sup>30</sup> indicating a non-porous or macroporous solid. The isotherms of the other catalysts were characteristic of mesoporous materials classified as type IV with the  $\text{H}_2$  hysteresis loop. The combustion method generated materials having a specific surface area

**Table 3.** Porosity,  $\text{CO}_2$  Adsorption Capacity, Crystallite Size, and I2/I1 Ratio of Different Catalysts

catalysts	$S_{\text{BET}}/\text{m}^2\text{g}^{-1}$	$V_{\text{pore}}/\text{cm}^3\text{g}^{-1}$	$\text{CO}_2$ adsorbed/ $\mu\text{mol g}^{-1}$	crystallite size <sup>a</sup> /nm	I2/ I1 <sup>b</sup>
I-comb	4.4	0.008	55	39	0.64
I-hydro	47.4	0.095	149	12	0.95
I-ammo	54.8	0.128	274	13	0.78
I-carb	32.5	0.139	195	19	0.71
IZ-comb	5.2	0.012	78	29	0.80
IZ-hydro	58.4	0.145	242	16	0.91
IZ-ammo	69.6	0.184	399	12	0.96
IZ-carb	69.3	0.298	509	13	0.93

<sup>a</sup>Calculated from the Scherrer equation for the (431) plane. <sup>b</sup>From Raman analysis, where I2 and I1 are the intensity of the bands at 369 and 308  $\text{cm}^{-1}$ , respectively.

significantly lower than those prepared by urea hydrolysis and precipitation. The specific surface areas of the I-comb and IZ-comb were 4.4 and 5.2  $\text{m}^2\text{g}^{-1}$ , respectively (Table 2). These values were about 10–15-fold lower than those of their counterparts, e.g., 47.4  $\text{m}^2\text{g}^{-1}$  of I-hydro and 69.6  $\text{m}^2\text{g}^{-1}$  of IZ-ammo. Remarkably, the mixed oxides of  $\text{In}_2\text{O}_3\text{-ZrO}_2$  catalysts always had higher specific surface areas than their  $\text{In}_2\text{O}_3$  counterparts for all four synthesis methods. This implied that the inclusion of  $\text{ZrO}_2$  improved the specific surface area of the catalysts. It is also worth noting that the synthesis method

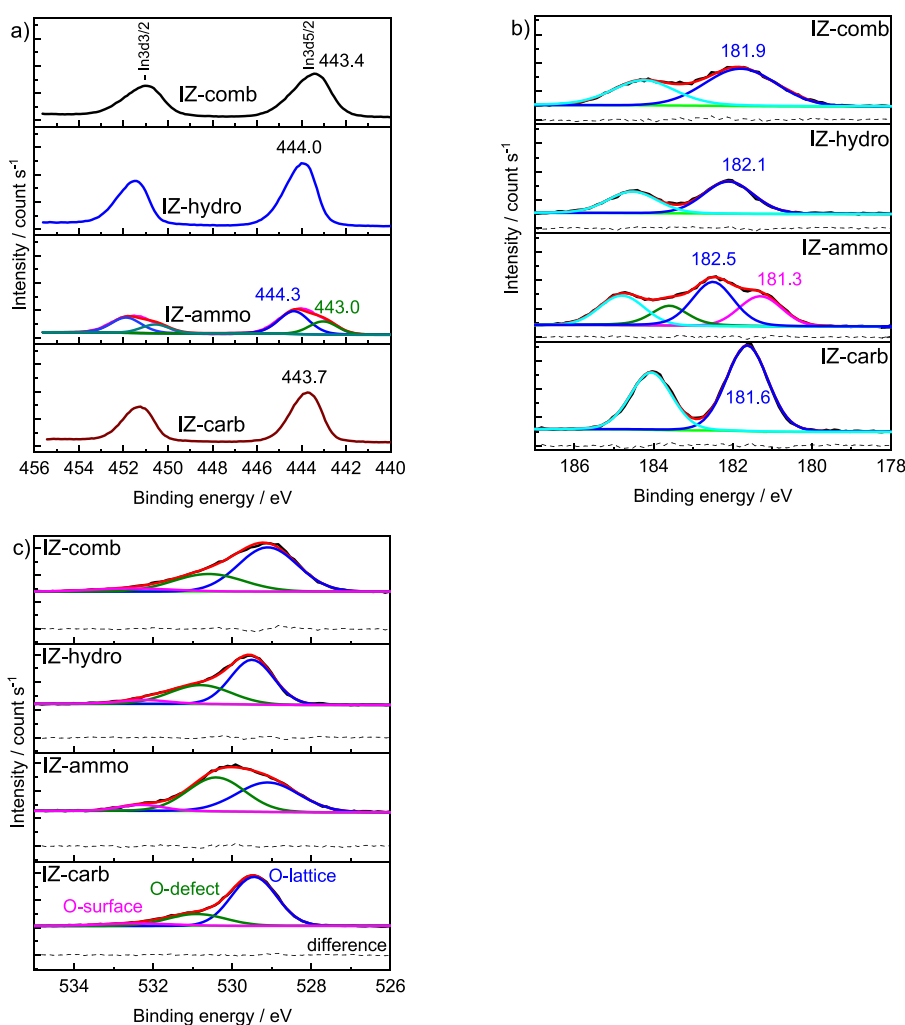


**Figure 5.** XPS spectra of  $\text{In}_2\text{O}_3\text{-ZrO}_2$  catalysts: (a) In 3d; (b) Zr 3d, and (c) O 1s core level.

significantly influenced the pore size distribution of the materials (Figures S6b and S7b). The average pore size decreased in the order of urea hydrolysis < precipitation with ammonia < precipitation with  $\text{Na}_2\text{CO}_3$  for both  $\text{In}_2\text{O}_3$  and  $\text{In}_2\text{O}_3\text{-ZrO}_2$  series.

Figure 5 presents the XPS spectra of In 3d, O 1s, and Zr 3d core levels of different  $\text{In}_2\text{O}_3\text{-ZrO}_2$  catalysts. The In 3d core levels of all samples exhibited two well-separated spin-orbits with a characteristic separation of 7.6 eV between the In 3d5/2 and In 3d3/2 components. The shape of the peaks and the maximum positions of the In 3d5/2 core levels were different between the samples (Figure 5a). The peaks were more asymmetric for IZ-ammo than for the other  $\text{In}_2\text{O}_3\text{-ZrO}_2$  samples. The IZ-comb showed the In 3d5/2 peak at approximately 443.4 eV which was much lower than the value of 443.7 eV for IZ-carb, 444.0 eV for IZ-hydro and 444.3 eV for IZ-ammo. It can be noted that the assignment of the oxidation state for In in  $\text{In}_2\text{O}_3$  is discrepant in the literature. For example, the database of XPS of the National Institute of Standards and Technology (NIST) assigned a binding energy of In 3d5/2 from 443.2 to 444.0 eV for metallic indium ( $\text{In}^0$ ).<sup>31</sup> In contrast, in the database of Thermofisher, the BEs at 443.8 and 444.0 were assigned to  $\text{In}^0$  and  $\text{In}^{3+}$  ( $\text{In}_2\text{O}_3$ ), respectively.<sup>32</sup> It should be noted that the accompanying “loss energy” at around 455–456 eV, a characteristic feature of the metallic indium spectrum, was not observed in any of the four

samples. Therefore, it is unlikely to interpret these results as a dominant presence of  $\text{In}^0$ , for the case of IZ-comb with the lowest BE of In 3d5/2 at 443.4 eV. It should also be noted that with XRD analysis (a technique for bulk analysis) the main phase in these samples was indium oxide, whereas XPS is a surface technique that can analyze the state of material only a few nanometers from the surface. A relatively low value of BE of In 3d5/2 for IZ-comb indicated that there was less electron density around In on the surface (depth up to 5–6 nm, reference<sup>14</sup> and this seemed to be characteristic of the combustion method because the I-comb sample had a similar value of binding energy of In 3d5/2 (443.5 eV) (Figure S8a). Interestingly, the  $\text{In}_2\text{O}_3$  prepared by thermal decomposition of the  $\text{In}(\text{NO}_3)_3$  precursor also showed a similar value of In 3d5/2 at 443.6 eV in the literature.<sup>33</sup> To clarify that a shift to the lower binding energy of the I-comb sample was not because of the instrumentation issue, we also performed the measurements for other indium oxide samples. As shown in Figure S8a, all three samples (I-hydro, I-ammo, and I-carb) showed a binding energy of In 3d5/2 of around 444.0 eV. We hypothesize that a small fraction of In on the surface of  $\text{In}_2\text{O}_3$  in the I-comb sample is loosely bonded with oxygen, giving BEs close to metallic In. It should be noted that in the In 3d5/2 of IZ-ammo, the peak at BE of 444.3 eV is the dominant peak at 443.0 eV, indicating that the fraction of the oxide form on the surface of this material was higher than that for the

others. This could indicate a strong interaction between  $\text{In}_2\text{O}_3$  and  $\text{ZrO}_2$  due to the formation of a solid solution.

The spectra of the Zr 3d5/2 core level are different among the samples (Figure 5b). Three spectra of IZ-comb, IZ-hydro, and IZ-carb showed a symmetric peak at approximately 181.9, 182.1, and 181.6 eV, respectively, whereas the spectrum of IZ-ammo was broad and asymmetric, which could be deconvoluted into two peaks at 182.5 and 181.3 eV. For four samples, the BE values of the main peaks from 181.6 to 182.4 eV were close to the binding energy of Zr 3d5/2 of tetragonal  $\text{ZrO}_2$ ,<sup>34</sup> in agreement with the XRD data. A deviation of the BEs between the samples indicated a difference in the electron density around  $\text{Zr}^{4+}$ . The second peak at 181.3 eV in the 3d5/2 spectrum of IZ-ammo indicated the presence of Zr species with less electron density ( $\text{Zr}^{\delta+}$ ) which was likely associated with the presence of oxygen defects. It should be noted that the binding energy of Zr 3d of pure  $\text{ZrO}_2$  depended on the morphology in which the BE of Zr 3d of monoclinic  $\text{ZrO}_2$  was lower than that of tetragonal  $\text{ZrO}_2$ .<sup>35</sup> It could not be discarded that there is evidence of a trace of a monoclinic phase on the surface because the sample of only  $\text{ZrO}_2$  using the same method showed a mixed phase of both monoclinic and tetragonal (Figure S4). Notably, the characteristics of Zr 3d5/2 seemed to coincide with the features of In 3d5/2 of the IZ-ammo, suggesting an interaction between  $\text{In}_2\text{O}_3$  and  $\text{ZrO}_2$  in this sample. Indeed, this interaction was confirmed by the interpretation of the O 1s.

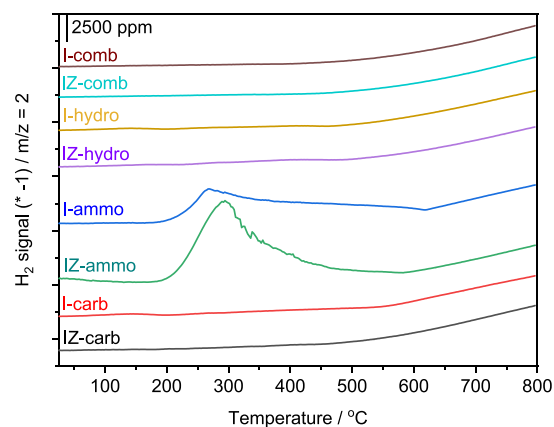
The O 1s spectrum of IZ-ammo showed a significant difference in shape compared to the others (Figure 5c). In the O 1s spectrum, three binding energies at approximately 532.3, 530.5, and 529.1 eV were ascribed to the surface (e.g.,  $-\text{OH}$  group), defect, and lattice oxygen, respectively.<sup>36</sup> Notably, the oxygen defect accounted for 47% of the IZ-ammo which was significantly higher than those for the other three catalysts (23–35%) (Table 4). This result is consistent with the highest

**Table 4. Percentage of Different Oxygen (O) Species Deconvoluted from O 1s Binding Energy**

sample	lattice O (%)	O-defect (%)	surface O (%)
I-comb	72	17	11
I-hydro	68	21	11
I-ammo	71	17	12
I-carb	75	14	11
IZ-comb	64	30	6
IZ-hydro	59	34	7
IZ-ammo	46	47	7
IZ-carb	71	23	6

content of the defect interpreted from Raman data in which the highest ratio of I2/I1 = 0.96 was found on the IZ-ammo catalyst (Table 3). It is also observed that the ratio between surface  $-\text{OH}$  and O-defect was significantly different between  $\text{In}_2\text{O}_3$  and  $\text{In}_2\text{O}_3\text{-ZrO}_2$  counterparts (Table 4). For the  $\text{In}_2\text{O}_3$  series, the percentage of O-defect and surface  $-\text{OH}$  was around 14–21% and 11–12%, respectively. Whereas for the  $\text{In}_2\text{O}_3\text{-ZrO}_2$  samples, the former increased by 1.6–2.8-fold while the latter decreased by 1.6–1.8-fold.

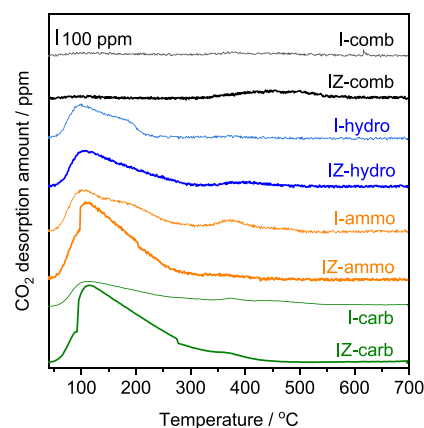
Figure 6 presents the  $\text{H}_2$ -TPR profiles of different catalysts. Pure  $\text{ZrO}_2$  showed a negligible consumption of  $\text{H}_2$  with a flat profile during the analysis. The profile of all  $\text{In}_2\text{O}_3$  and  $\text{In}_2\text{O}_3\text{-ZrO}_2$  samples showed only one reduction feature at a high-temperature range of 400–800 °C, whereas the profile of I-



**Figure 6.**  $\text{H}_2$ -TPR profiles  $\text{In}_2\text{O}_3$  and  $\text{In}_2\text{O}_3\text{-ZrO}_2$  prepared by different synthesis methods.

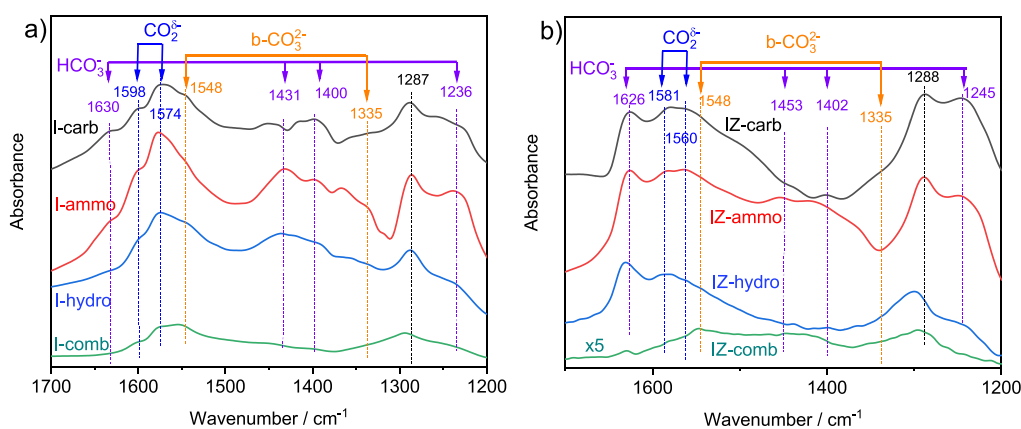
ammo had also another peak at around 270–295 °C. The peak at low temperatures is associated with the reduction of surface  $\text{In}_2\text{O}_3$  while the peak at high temperatures could be attributed to the reduction of bulk  $\text{In}_2\text{O}_3$ . The profiles of IZ samples showed similar features as their pure  $\text{In}_2\text{O}_3$  counterparts. The synthesis method using ammonia solution as the precipitating agent facilitates a reduction of  $\text{In}_2\text{O}_3$  at lower temperatures, contrary to all the other preparation methods. The easy reduction at low temperatures for I-ammo and IZ-ammo is perhaps related to their higher content of oxygen defects which is consistent with the Raman and XPS analysis.<sup>14</sup> Additionally, the reduction of  $\text{ZrO}_2$  was also negligible compared to  $\text{In}_2\text{O}_3$  and  $\text{In}_2\text{O}_3\text{-ZrO}_2$  (Figure S9).

Figure 7 presents the  $\text{CO}_2$ -TPD profiles for different catalysts. The profile for both I-comb and IZ-comb were



**Figure 7.**  $\text{CO}_2$ -TPD profiles of  $\text{In}_2\text{O}_3$  and  $\text{In}_2\text{O}_3\text{-ZrO}_2$  prepared by different synthesis methods.

almost flat resulting in a small  $\text{CO}_2$  uptake of 55 and 78  $\mu\text{mol g}^{-1}$ , respectively. By contrast, the profiles of I-ammo, I-hydro, and I-carb showed one broad peak centered at around 105 °C and one weak peak at around 373 °C. Their  $\text{CO}_2$  uptakes were 3-fold to 5-fold higher than that of the I-comb (Table 3). The  $\text{In}_2\text{O}_3\text{-ZrO}_2$  samples had a similar shape of the  $\text{CO}_2$ -TPD profile to their  $\text{In}_2\text{O}_3$  counterparts; however, the profiles were more intense. As a result, the  $\text{CO}_2$  uptakes of the IZ samples were about 41–62% higher than those of the pure  $\text{In}_2\text{O}_3$  counterparts (Table 3). This implies that  $\text{ZrO}_2$  supports an



**Figure 8.** In situ DRIFTS spectra of different catalysts, (a)  $\text{In}_2\text{O}_3$  and (b)  $\text{In}_2\text{O}_3\text{-ZrO}_2$  after 90 min adsorption of  $\text{CO}_2$  at  $35\text{ }^\circ\text{C}$  (gas flow ( $100\text{ mL min}^{-1}$ ) of  $2000\text{ ppm}$  of  $\text{CO}_2/\text{Ar}$ ).

enhanced  $\text{CO}_2$  adsorption capacity of the mixed oxide catalysts compared to the single  $\text{In}_2\text{O}_3$  samples.

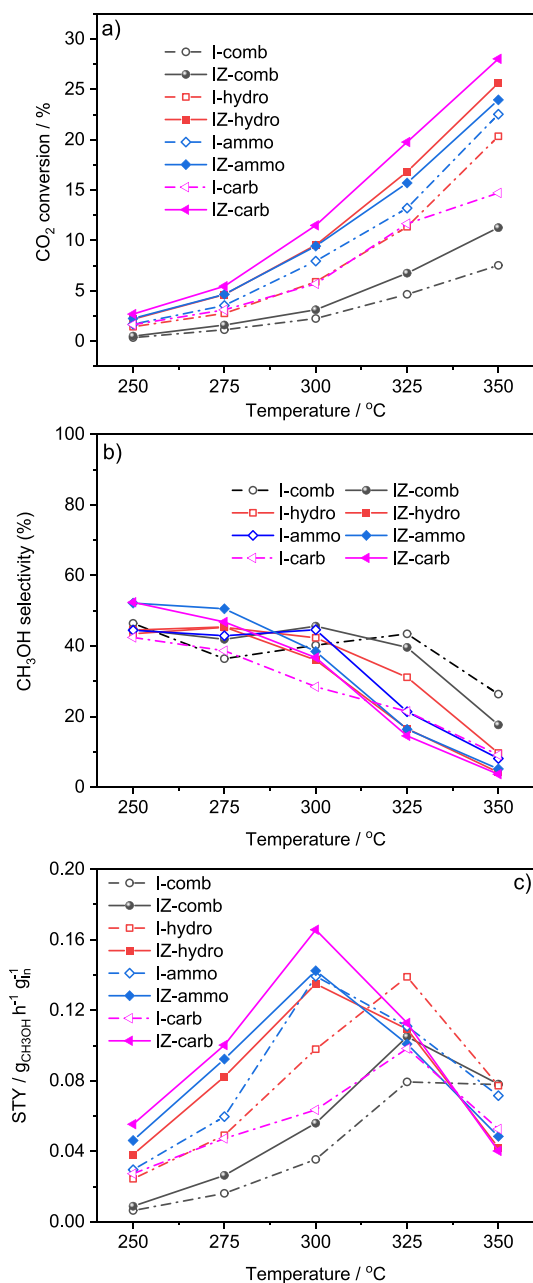
To gain further information on the structural effect of the catalysts on  $\text{CO}_2$  activation, DRIFTS measurements were performed in situ during  $\text{CO}_2$  adsorption over the catalysts. Figure 8 presents the IR spectra of  $\text{In}_2\text{O}_3$  and  $\text{In}_2\text{O}_3\text{-ZrO}_2$  after the adsorption of  $\text{CO}_2$  for 90 min. It is known that  $\text{CO}_2$  can use its oxygens or electrophilic carbon to interact with the surface  $\text{-OH}$  and oxygen vacancies of the catalysts in complex coordination (symmetrical, monodentate, bidentate, and bridged configurations).<sup>37</sup> These interactions possibly form bicarbonates, carbonates, carboxylates, and linear  $\text{CO}_2$  species.<sup>38</sup> Different interpretations have been used to assign each species in the literature due to peak overlap and dependence on types of metal oxides. Herein, to simplify the interpretation, we focus on pointing out the different characteristics of the catalysts during  $\text{CO}_2$  adsorption to investigate the effect of the catalyst preparation method. As shown in Figure 8a, all spectra showed similar shapes in which the bands positioned at  $1630$ ,  $1431$ , and  $1236\text{ cm}^{-1}$  can be assigned to bicarbonate ( $\text{HCO}_3^-$ ) with the IR modes of  $\nu_{\text{as}}(\text{CO}_3)$ ,  $\nu_{\text{s}}(\text{CO}_3)$ , and  $\delta(\text{HO})$ , respectively.<sup>39</sup> The two bands at  $1598$  and  $1574\text{ cm}^{-1}$  are possibly attributed to two types of carboxylate species ( $\text{CO}_2^{\delta-}$ ), while the bands at around  $1548$  and  $1335\text{ cm}^{-1}$  are assigned to bidentate carbonate ( $\text{b-CO}_3^{2-}$ ).<sup>38,40</sup> It should be noted that the overlap of the peaks in the locations around  $1600\text{ cm}^{-1}$  makes it challenging to assign the species. Indeed, the bands at  $1598$  and  $1574\text{ cm}^{-1}$  can be also assigned to formate intermediate species or bidentate carbonates in the literature.<sup>19,40</sup> Additionally, there was one intense peak at around  $1287\text{ cm}^{-1}$  which was also observed by Yan et al. for  $\text{CO}_2$  adsorption on indium oxide.<sup>41</sup> Unfortunately, the authors did not assign this peak. However, this peak can possibly belong to bidentate carbonates as reported for  $\text{CO}_2$  adsorption on  $\text{Ni/CeO}_2$ .<sup>42</sup> The spectrum of the I-comb sample was much less intense than the others, probably due to the low specific surface area and hence the low adsorption capacity of  $\text{CO}_2$  on this catalyst.

The spectra for the binary oxides  $\text{In}_2\text{O}_3\text{-ZrO}_2$  also showed similar carbonate species as those of  $\text{In}_2\text{O}_3$  samples, although there were some shifts in the peak positions. This can be explained by a difference in electron density due to the presence of  $\text{ZrO}_2$ . However, the most different characteristic was the peak at around  $1626\text{ cm}^{-1}$ . It was much more intense for  $\text{In}_2\text{O}_3\text{-ZrO}_2$  than the  $\text{In}_2\text{O}_3$  counterpart. This indicates

that more bicarbonate species ( $\text{HCO}_3^-$ ) were formed on  $\text{In}_2\text{O}_3\text{-ZrO}_2$  than  $\text{In}_2\text{O}_3$  during the  $\text{CO}_2$  adsorption.

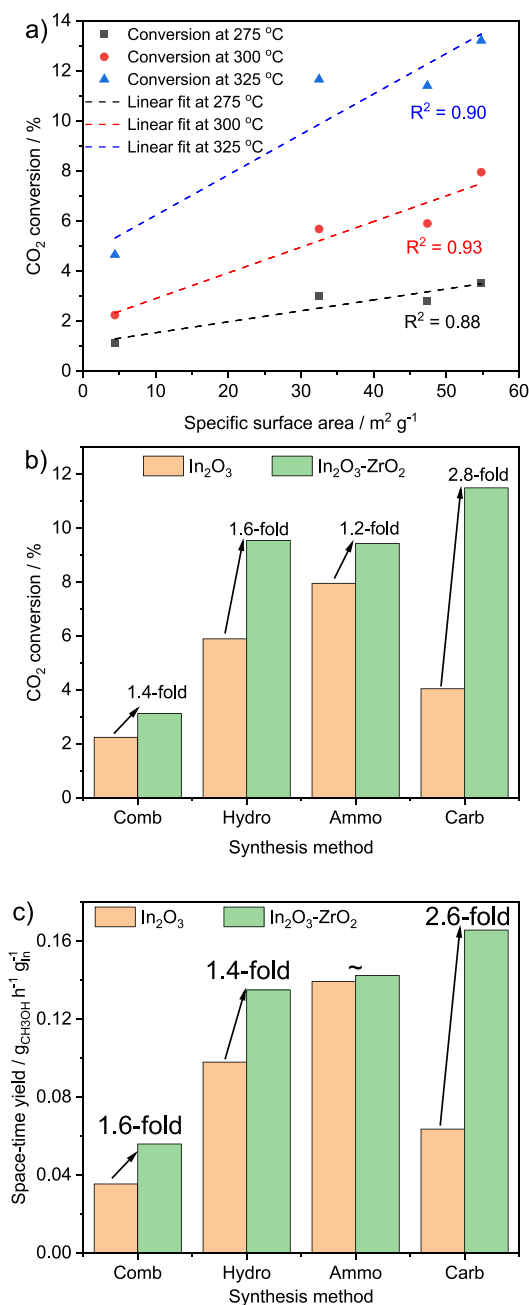
**3.2. Catalytic Activity.** The catalytic activity of the different catalysts for  $\text{CO}_2$  hydrogenation was examined in a fixed-bed reactor operated in a temperature range from  $250$  to  $350\text{ }^\circ\text{C}$  and pressure of  $40\text{ bar}$ . The mass of each catalyst was normalized to obtain the same amount of  $500\text{ mg}$  of indium for comparison purposes. In all the catalytic tests,  $\text{CH}_3\text{OH}$  and  $\text{CO}$  were the main products, whereas  $\text{CH}_4$  was only found in some cases. In those cases, however, the maximum selectivity of  $\text{CH}_4$  was less than  $2.5\%$ , and hence, the selectivity for  $\text{CH}_4$  is not reported in the results. The comparison of the catalytic activity between the catalysts was assessed in terms of  $\text{CO}_2$  conversion ( $X_{\text{CO}_2}$ ),  $\text{CH}_3\text{OH}$  selectivity ( $S_{\text{CH}_3\text{OH}}$ ), and space-time yield of  $\text{CH}_3\text{OH}$  ( $\text{STY}_{\text{CH}_3\text{OH}}$ ).

Figure 9 presents the activity performance ( $\text{CO}_2$  conversion, methanol selectivity, and space-time yield of methanol) of  $\text{In}_2\text{O}_3$  and  $\text{In}_2\text{O}_3\text{-ZrO}_2$  prepared by combustion, urea hydrolysis, and precipitation with  $\text{NH}_4\text{OH}$  solution. More detailed information on methanol yield and  $\text{CO}$  selectivity are presented in Figure S10. For all catalysts,  $\text{CO}_2$  conversion increased substantially as temperature increased from  $250$  to  $350\text{ }^\circ\text{C}$  (Figure 9a). For catalysts containing solely  $\text{In}_2\text{O}_3$ , the  $\text{CO}_2$  conversion increased in the order of  $\text{I-comb} \ll \text{I-hydro} \approx \text{I-carb} < \text{I-ammo}$ . The  $\text{CO}_2$  conversions linearly correlate with the specific surface areas (Figure 10a), suggesting the specific surface area plays a crucial role in the  $\text{CO}_2$  conversion since all four catalysts had the same cubic structure of  $\text{In}_2\text{O}_3$ . Significantly lower conversion of  $\text{CO}_2$  on the I-comb catalyst was accounted for by a substantially lower specific surface area of the catalyst. It is noted that the  $\text{CO}_2$  conversions of I-carb, I-hydro, and I-ammo are better to some extent than those reported in the literature under similar or milder reaction conditions (Table 5). For example,  $\text{In}_2\text{O}_3$  prepared by the precipitation with  $\text{Na}_2\text{CO}_3$  showed a conversion of  $11.8\%$  at  $350\text{ }^\circ\text{C}$  under similar reaction conditions,<sup>22</sup> whereas other studies reported much lower  $\text{CO}_2$  conversion even under milder reaction conditions (e.g., lower WHSH, reactants diluted with inert gases).<sup>43,44</sup> Both I-hydro and I-ammo catalysts showed a  $\text{CH}_3\text{OH}$  selectivity of  $42\text{--}45\%$  for temperatures  $250\text{--}300\text{ }^\circ\text{C}$  and the selectivity decreased rapidly with a further increase in temperature due to the RWGS reaction being increasingly thermodynamically favored. The I-comb catalyst also had a similar value of  $\text{CH}_3\text{OH}$  selectivity as I-hydro and I-ammo at temperatures from  $250$  to  $350\text{ }^\circ\text{C}$  but it



**Figure 9.** Comparison of In<sub>2</sub>O<sub>3</sub> and In<sub>2</sub>O<sub>3</sub>-ZrO<sub>2</sub> catalysts for (a) CO<sub>2</sub> conversion, (b) CH<sub>3</sub>OH selectivity, and (c) STY of CH<sub>3</sub>OH.

lost CH<sub>3</sub>OH selectivity when the temperature was higher than 325 °C. The yield of CH<sub>3</sub>OH production on each catalyst is a trade-off between the CO<sub>2</sub> conversion and CH<sub>3</sub>OH selectivity (Figure 9b) due to a competition between the methanol generation reaction and the RWGS reaction. As a result, the maximum CH<sub>3</sub>OH production rate calculated per gram of Indium ( $g_{\text{CH}_3\text{OH}} g_{\text{In}}^{-1} \text{h}^{-1}$ ), i.e. methanol STY, was found to rank in the increasing order of I-comb (0.08 at 325 °C) < I-carb (0.10 at 325 °C) < I-hydro (0.14 at 325 °C) < I-ammo (0.14 at 300 °C) (Figure 9c). This implies that the preparation method strongly influences the catalytic performance for CO<sub>2</sub> hydrogenation to CH<sub>3</sub>OH. In the literature, CO<sub>2</sub> conversion, methanol selectivity, and methanol formation are usually correlated to the content of O vacancies;<sup>10,45</sup> however, in this work, the correlation between O vacancies and the methanol production rate was not clear.



**Figure 10.** (a) Correlation between the specific surface area and CO<sub>2</sub> conversion on In<sub>2</sub>O<sub>3</sub> prepared by various synthesis methods and (b) comparison of CO<sub>2</sub> conversion and (c) comparison of STY of methanol productivity on In<sub>2</sub>O<sub>3</sub> and In<sub>2</sub>O<sub>3</sub>-ZrO<sub>2</sub>.

Each In<sub>2</sub>O<sub>3</sub>-ZrO<sub>2</sub> mixed oxide catalyst prepared by the four different methods showed higher CO<sub>2</sub> conversion than that of its In<sub>2</sub>O<sub>3</sub> counterpart (Figure 9a, the solid line versus the dashed line with the same color). In particular, the CO<sub>2</sub> conversions on the In<sub>2</sub>O<sub>3</sub>-ZrO<sub>2</sub> catalysts were 1.2 to 2.8-fold higher than their In<sub>2</sub>O<sub>3</sub> counterparts (Figure 10b). This indicates a clear advantage of ZrO<sub>2</sub> support in the mixed oxide In<sub>2</sub>O<sub>3</sub>-ZrO<sub>2</sub> catalysts, which is generally related to the improvement in CO<sub>2</sub> adsorption capacity and oxygen vacancies of the In<sub>2</sub>O<sub>3</sub>-ZrO<sub>2</sub> catalysts than their In<sub>2</sub>O<sub>3</sub> counterparts.<sup>14,20,29</sup> In fact, in our cases, all samples of binary oxides In<sub>2</sub>O<sub>3</sub>-ZrO<sub>2</sub> exhibited higher CO<sub>2</sub> adsorption capacity than single In<sub>2</sub>O<sub>3</sub> counterparts (Table 3). Moreover, a similar trend

Table 5. Comparison of the Activity Performance of the Catalysts Reported in This Study and the Recent Literature

catalysts	CO <sub>2</sub> /H <sub>2</sub> /inert (v/v)	space velocity		pressure (MPa)	temperature (K)	CO <sub>2</sub> conversion (%)	CH <sub>3</sub> OH formation		ref
		GHSV (h <sup>-1</sup> )	WHSV (L g <sup>-1</sup> h <sup>-1</sup> )				STY (mmol g <sub>cat</sub> <sup>-1</sup> h <sup>-1</sup> )	selectivity (%)	
In <sub>2</sub> O <sub>3</sub>	1/4	16,000	26	5	573		ca. 6.3	100	9
In <sub>2</sub> O <sub>3</sub> /ZrO <sub>2</sub>	1/4	16,000	26	5	573	5.2	9.2	100	9
In <sub>2.5</sub> /ZrO <sub>2</sub>	1/4/1.67	24,000		5	523	0.9	1.1	74	18
hexagonal-In <sub>2</sub> O <sub>3</sub>	1/3/0.55		21.6	4	598	4.4	6.3	68	46
1.5Y9In/ZrO <sub>2</sub>	1:4/1.5		52	4	573	7.6	13.1	69	47
3La10In/ZrO <sub>2</sub>	1/4/1.5		52	4	573	7.7	13.1	66	47
In <sub>2</sub> O <sub>3</sub>	1/3/1		9	2	593	~5	14.6	~39	44
20In/ZrO <sub>2</sub> -800	1/3/1		9	2	593	~5	59.6	~51	44
c-In <sub>2</sub> O <sub>3</sub>	1/4/0		16	4	613	~12	3.0	20	43
rh-In <sub>2</sub> O <sub>3</sub>	1/4/0		16	4	613	~5	1.8	30	43
In <sub>2</sub> O <sub>3</sub> - commercial	1/3/1		15	4	543	1.1	0.8	55	8
In <sub>2</sub> O <sub>3</sub> - commercial	1/3/1		15	4	603	7.1	3.7	40	8
cubic-In <sub>2</sub> O <sub>3</sub>	1/3/1		7.5	3	573	~4.2	1.99	~70	13
hexagonal-In <sub>2</sub> O <sub>3</sub>	1/3/1		7.5	3	573	~4.8	2.32	~70	13
In <sub>2</sub> O <sub>3</sub> -hydro	1/3/0		12	4	598	11.4	3.6	31	this work
In <sub>2</sub> O <sub>3</sub> -ZrO <sub>2</sub> - carb	1/3/0		12	4	573	11.5	3.0	37	this work
In <sub>2</sub> O <sub>3</sub> -ZrO <sub>2</sub> - hydro	1/3/0		12	4	573	9.5	2.4	36	this work

was found for indirect evidence of oxygen vacancies (I2/I1 ratio from Raman analysis) except for the pair of I-hydro and IZ-hydro (Table 3). However, it should be noted that in the case of I-hydro and IZ-hydro, a difference in the phase of In<sub>2</sub>O<sub>3</sub> (cubic and rhombohedral, Figure 1a) could play a role in the catalytic activity. IZ-hydro and IZ-ammo catalysts showed very similar CO<sub>2</sub> conversion up to 300 °C but IZ-hydro is slightly better than IZ-ammo at higher temperatures (Figure 9a). Both catalysts outperformed the IZ-comb for the conversion of CO<sub>2</sub> from 250 to 350 °C. Noticeably, the IZ-carb was the best among the four samples of In<sub>2</sub>O<sub>3</sub>-ZrO<sub>2</sub>. This catalyst had 11.5% conversion of CO<sub>2</sub>, 37% selectivity for CH<sub>3</sub>OH (and hence a maximum 4.2% yield of CH<sub>3</sub>OH, Figure S10a) at 300 °C, giving a methanol STY of 0.17 g<sub>CH<sub>3</sub>OH</sub> g<sub>In<sub>2</sub>O<sub>3</sub></sub><sup>-1</sup> h<sup>-1</sup>. The best activity of IZ-carb may be related to its textural properties (Figure 10c), for example, large specific surface area and substantially larger CO<sub>2</sub> adsorption capacity compared to those of the others (see Table 3). Moreover, the pore width (and subsequently the total pore volume) may also play a role because this is the only different textural property between IZ-carb and IZ-ammo, where IZ-carb had 0.298 cm<sup>3</sup> g<sup>-1</sup> while IZ-ammo had 0.184 cm<sup>3</sup> g<sup>-1</sup>.

It should be noted that the sodium carbonate precipitation synthesis was the most favorable for the ZrO<sub>2</sub>-supported catalyst performance but among the least favorable for the unsupported In<sub>2</sub>O<sub>3</sub> catalyst series. A larger crystallite size was found by XRD for I-carb than I-ammo and I-hydro which accounted for a lower specific surface area of I-carb than their counterparts (I-ammo and I-hydro) (Table 3). In the presence of cation Zr<sup>4+</sup>, all three catalysts prepared by coprecipitation and urea hydrolysis exhibited a high specific surface area, but the difference in the pore width distribution in which the IZ-carb catalyst had a larger value of the average pore width. This indicates that the preparation method significantly influences the CO<sub>2</sub> conversion for In<sub>2</sub>O<sub>3</sub>-ZrO<sub>2</sub> catalysts. The IZ-hydro and IZ-ammo catalysts showed a maximum rate of CH<sub>3</sub>OH

STY (at 300 °C) of approximately 0.135 and 0.142 g<sub>CH<sub>3</sub>OH</sub> g<sub>In<sub>2</sub>O<sub>3</sub></sub><sup>-1</sup> h<sup>-1</sup>, respectively, whereas IZ-comb had its maximum rate of CH<sub>3</sub>OH STY of about 0.104 g<sub>CH<sub>3</sub>OH</sub> g<sub>In<sub>2</sub>O<sub>3</sub></sub><sup>-1</sup> h<sup>-1</sup> at 325 °C. It is noted that the IZ-hydro had a mixed phase of rhombohedral and cubic In<sub>2</sub>O<sub>3</sub> while IZ-ammo possessed only cubic In<sub>2</sub>O<sub>3</sub>. A slightly higher CO<sub>2</sub> conversion and methanol yield on I-ammo (only cubic phase) than I-hydro (cubic and trace of rhombohedral phase) suggests that the cubic phase of In<sub>2</sub>O<sub>3</sub> might be better than the rhombohedral phase as reported in the literature.<sup>13</sup> Yang and co-workers found that the cubic In<sub>2</sub>O<sub>3</sub> had a larger production of methanol than rhombohedral unsupported In<sub>2</sub>O<sub>3</sub> although the former showed lower methanol selectivity than the latter.<sup>43</sup>

The apparent activation energy of CO<sub>2</sub> on each catalyst was calculated from the slope of the fitted linear regression of the Arrhenius plots, as shown in Figure 11. The apparent activation energies of all catalysts prepared by precipitation and hydrolysis methods were in the range of 71–77 kJ/mol, whereas the values of two samples I-comb and IZ-comb prepared by the combustion method were around 90–91 kJ/mol. This indicates that the pathway of CO<sub>2</sub> activation on the I-comb and IZ-comb was different than other catalysts. The finding was consistent with DRIFTS data in which there were much less –CO<sub>3</sub> species formed on I-comb and IZ-comb catalysts during the adsorption of CO<sub>2</sub>.

#### 4. CONCLUSIONS

In<sub>2</sub>O<sub>3</sub> and In<sub>2</sub>O<sub>3</sub>-ZrO<sub>2</sub> materials were synthesized by various preparation methods including those with urea and ammonia (free-alkaline) (urea combustion, urea hydrolysis, precipitation with ammonia/ethanol) and the precipitation with sodium carbonate. The preparation methods strongly affected the properties of the catalysts. The combustion method produced a separate phase of ZrO<sub>2</sub> causing a very low specific surface area and, as a result, the catalytic performance of the materials was also limited. A reassembled structure of cubic In<sub>2</sub>O<sub>3</sub> for the

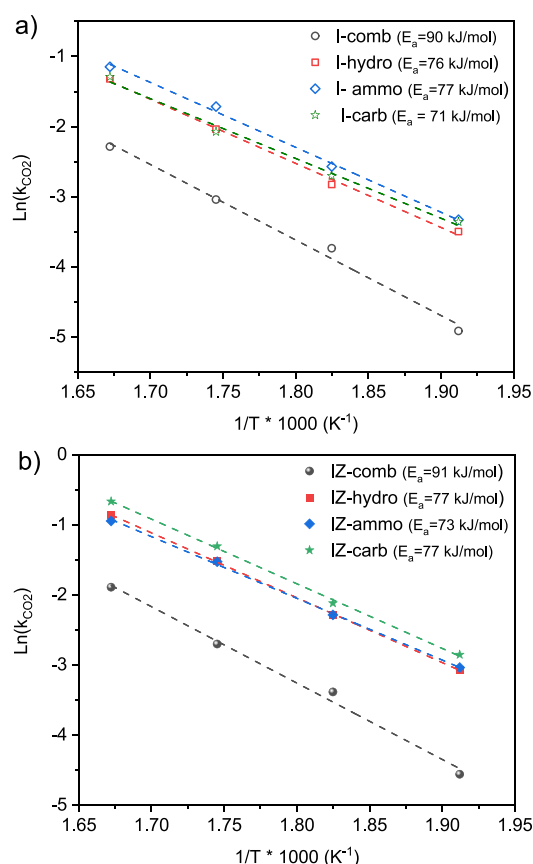


**Figure 11.** Arrhenius plot for different  $\text{In}_2\text{O}_3$  and  $\text{In}_2\text{O}_3\text{-ZrO}_2$  catalysts. Apparent activation energy ( $E_a$ ) was calculated from the slope of the linear regression. All conversion values used in the calculations were lower than 20% to ensure that the selected temperature was in the kinetic range.

$\text{In}_2\text{O}_3\text{-ZrO}_2$  catalysts prepared by the precipitation with ammonia/ethanol and sodium carbonate indicated a strong interaction between  $\text{In}_2\text{O}_3$  and  $\text{ZrO}_2$ . In contrast, the urea hydrolysis method also generated the rhombohedral  $\text{In}_2\text{O}_3$  structure in both I-hydro and IZ-hydro. The highest content of oxygen defects was found in the  $\text{In}_2\text{O}_3\text{-ZrO}_2$  sample prepared by the precipitation with ammonia/ethanol. However, this factor did not guarantee the best activity performance. The catalytic performance was mostly correlated to the specific surface area. For all preparation methods, the  $\text{In}_2\text{O}_3\text{-ZrO}_2$  mixed oxide catalysts had better performance than their  $\text{In}_2\text{O}_3$  counterparts. However, using the Na carbonate preparation, the performance was particularly strongly boosted with the mixed oxide. This was due to the IZ-carb catalyst's good textural properties, high  $\text{CO}_2$  adsorption capacity, and strong interaction between  $\text{In}_2\text{O}_3$  and  $\text{ZrO}_2$  (as observed from XRD).

## ■ ASSOCIATED CONTENT

### SI Supporting Information

The Supporting Information is available free of charge at <https://pubs.acs.org/doi/10.1021/acs.energyfuels.3c04721>.

TGA profiles of  $\text{In}(\text{NO}_3)_3 \cdot x\text{H}_2\text{O}$  and  $\text{ZrO}(\text{NO}_3)_2 \cdot y\text{H}_2\text{O}$  precursors; Optical image of  $\text{In}_2\text{O}_3$  prepared by urea combustion method; criteria for estimation of transport effects; XRD data of  $\text{ZrO}_2$  samples prepared by different methods; SEM/EDX measurements of selected  $\text{In}_2\text{O}_3\text{-ZrO}_2$  catalysts;  $\text{N}_2$  physisorption data of  $\text{In}_2\text{O}_3$  and

$\text{In}_2\text{O}_3\text{-ZrO}_2$ ; XPS data of all  $\text{In}_2\text{O}_3$  samples;  $\text{H}_2$ -TPR profiles of  $\text{In}_2\text{O}_3$ ,  $\text{ZrO}_2$ , and  $\text{In}_2\text{O}_3\text{-ZrO}_2$  prepared by urea synthesis; and comparison of  $\text{CH}_3\text{OH}$  yield and  $\text{CO}$  selectivity between  $\text{In}_2\text{O}_3$  and  $\text{In}_2\text{O}_3\text{-ZrO}_2$  catalysts (PDF)

## ■ AUTHOR INFORMATION

### Corresponding Authors

**Patricia Benito** – Dipartimento di Chimica Industriale “Toso Montanari”, University of Bologna, Bologna 40136, Italy; [orcid.org/0000-0003-0487-6782](https://orcid.org/0000-0003-0487-6782); Email: [patricia.benito3@unibo.it](mailto:patricia.benito3@unibo.it)

**Louise Olsson** – Chemical Engineering, Competence Centre for Catalysis, Chalmers University of Technology, Gothenburg SE-412 96, Sweden; [orcid.org/0000-0002-8308-0784](https://orcid.org/0000-0002-8308-0784); Email: [louise.olsson@chalmers.se](mailto:louise.olsson@chalmers.se)

### Authors

**Phuoc Hoang Ho** – Chemical Engineering, Competence Centre for Catalysis, Chalmers University of Technology, Gothenburg SE-412 96, Sweden

**Giovanni Tizzanini** – Dipartimento di Chimica Industriale “Toso Montanari”, University of Bologna, Bologna 40136, Italy

**Sreetama Ghosh** – CO<sub>2</sub> Research and Green Technologies Centre, Vellore Institute of Technology (VIT), Vellore, Tamil Nadu 632014, India

**Wei Di** – Chemical Engineering, Competence Centre for Catalysis, Chalmers University of Technology, Gothenburg SE-412 96, Sweden

**Jieling Shao** – Chemical Engineering, Competence Centre for Catalysis, Chalmers University of Technology, Gothenburg SE-412 96, Sweden

**Oleg Pajalic** – Perstorp Specialty Chemicals AB, Perstorp 284 80, Sweden

**Lars Josefsson** – Josefsson Sustainable Chemistry AB, Stenungsund 444 48, Sweden

**Derek Creaser** – Chemical Engineering, Competence Centre for Catalysis, Chalmers University of Technology, Gothenburg SE-412 96, Sweden; [orcid.org/0000-0002-5569-5706](https://orcid.org/0000-0002-5569-5706)

Complete contact information is available at:

<https://pubs.acs.org/doi/10.1021/acs.energyfuels.3c04721>

### Notes

The authors declare the following competing financial interest(s): Co-author: Oleg Pajalic reports a relationship with Perstorp Specialty Chemicals AB that includes: employment. Co-author: Lars Josefsson, employed by his own company Josefsson Sustainable Chemistry AB.

## ■ ACKNOWLEDGMENTS

This work was performed at the Competence Centre for Catalysis (KCK) and the Division of Chemical Engineering, Chalmers University of Technology in collaboration with Perstorp, Josefsson Sustainable Chemistry, and Chimica Industriale “Toso Montanari” at the University of Bologna. We thank the Swedish Energy Agency for financial support (Grant number P49617-1). Part of the characterization was conducted at the Chalmers Materials Analysis Lab (CMAL). We acknowledge the assistance from Dr. Eric Tam for XPS analysis and Dr. Katarina Logg for Raman measurements.

## REFERENCES

- (1) Rahman, F. A.; Aziz, M. M. A.; Saidur, R.; Bakar, W. A. W. A.; Hainin, M. R.; Putrajaya, R.; Hassan, N. A. Pollution to solution: Capture and sequestration of carbon dioxide (CO<sub>2</sub>) and its utilization as a renewable energy source for a sustainable future. *Renewable and Sustainable Energy Reviews* **2017**, *71*, 112–126.
- (2) De, S.; Dokania, A.; Ramirez, A.; Gascon, J. Advances in the Design of Heterogeneous Catalysts and Thermocatalytic Processes for CO<sub>2</sub> Utilization. *ACS Catal.* **2020**, *10* (23), 14147–14185.
- (3) Dalena, F.; Senatore, A.; Marino, A.; Gordano, A.; Basile, M.; Basile, A. Methanol Production and Applications: An Overview. In *Methanol*; Basile, A.; Dalena, F. Eds.; Elsevier, 2018; pp 3–28.
- (4) *News European Parliament Home Page*. <https://www.europarl.europa.eu/news/en/press-room/20230911IPR04913/70-of-jet-fuels-at-eu-airports-will-have-to-be-green-by-2050> (accessed October 2023).
- (5) Bradin, D. Process for producing renewable jet fuel compositions. WO2014008337A1, 2013.
- (6) Yao, B.; Xiao, T.; Makgae, O. A.; Jie, X.; Gonzalez-Cortes, S.; Guan, S.; Kirkland, A. I.; Dilworth, J. R.; Al-Megren, H. A.; Alshihri, S. M.; et al. Transforming carbon dioxide into jet fuel using an organic combustion-synthesized Fe-Mn-K catalyst. *Nat. Commun.* **2020**, *11* (1), 6395.
- (7) Ye, J.; Liu, C.; Mei, D.; Ge, Q. Active Oxygen Vacancy Site for Methanol Synthesis from CO<sub>2</sub> Hydrogenation on In<sub>2</sub>O<sub>3</sub>(110): A DFT Study. *ACS Catal.* **2013**, *3* (6), 1296–1306.
- (8) Sun, K.; Fan, Z.; Ye, J.; Yan, J.; Ge, Q.; Li, Y.; He, W.; Yang, W.; Liu, C.-J. Hydrogenation of CO<sub>2</sub> to methanol over In<sub>2</sub>O<sub>3</sub> catalyst. *Journal of CO<sub>2</sub> Utilization* **2015**, *12*, 1–6.
- (9) Martin, O.; Martin, A. J.; Mondelli, C.; Mitchell, S.; Segawa, T. F.; Hauert, R.; Drouilly, C.; Curulla-Ferré, D.; Pérez-Ramírez, J. Indium Oxide as a Superior Catalyst for Methanol Synthesis by CO<sub>2</sub> Hydrogenation. *Angew. Chem., Int. Ed.* **2016**, *55* (21), 6261–6265.
- (10) Wang, J.; Zhang, G.; Zhu, J.; Zhang, X.; Ding, F.; Zhang, A.; Guo, X.; Song, C. CO<sub>2</sub> Hydrogenation to Methanol over In<sub>2</sub>O<sub>3</sub>-Based Catalysts: From Mechanism to Catalyst Development. *ACS Catal.* **2021**, *11* (3), 1406–1423.
- (11) Baumgarten, R.; Naumann d'Alnoncourt, R.; Lohr, S.; Gioria, E.; Frei, E.; Fako, E.; De, S.; Boscagli, C.; Drief, M.; Schunk, S.; et al. Quantification and Tuning of Surface Oxygen Vacancies for the Hydrogenation of CO<sub>2</sub> on Indium Oxide Catalysts. *Chem. Ing. Techn.* **2022**, *94* (11), 1765–1775.
- (12) Wang, C. Y.; Dai, Y.; Pezoldt, J.; Lu, B.; Kups, T.; Cimalla, V.; Ambacher, O. Phase Stabilization and Phonon Properties of Single Crystalline Rhombohedral Indium Oxide. *Cryst. Growth Des.* **2008**, *8* (4), 1257–1260.
- (13) Shi, Z.; Tan, Q.; Wu, D. Mixed-Phase Indium Oxide as a Highly Active and Stable Catalyst for the Hydrogenation of CO<sub>2</sub> to CH<sub>3</sub>OH. *Ind. Eng. Chem. Res.* **2021**, *60* (9), 3532–3542.
- (14) Frei, M. S.; Mondelli, C.; Cesarini, A.; Krumeich, F.; Hauert, R.; Stewart, J. A.; Curulla Ferré, D.; Pérez-Ramírez, J. Role of Zirconia in Indium Oxide-Catalyzed CO<sub>2</sub> Hydrogenation to Methanol. *ACS Catal.* **2020**, *10* (2), 1133–1145.
- (15) Wu, H.; Xiong, S.; Liu, C.-J. Preparation of In<sub>2</sub>O<sub>3</sub>/ZrO<sub>2</sub> catalyst via DBD plasma decomposition of Zr(OH)<sub>4</sub> for CO<sub>2</sub> hydrogenation to methanol. *Catal. Today* **2023**, *423*, 114024.
- (16) Tsoukalou, A.; Abdala, P. M.; Armutlulu, A.; Willinger, E.; Fedorov, A.; Müller, C. R. Operando X-ray Absorption Spectroscopy Identifies a Monoclinic ZrO<sub>2</sub>:In Solid Solution as the Active Phase for the Hydrogenation of CO<sub>2</sub> to Methanol. *ACS Catal.* **2020**, *10* (17), 10060–10067.
- (17) Yang, C.; Pei, C.; Luo, R.; Liu, S.; Wang, Y.; Wang, Z.; Zhao, Z.-J.; Gong, J. Strong Electronic Oxide–Support Interaction over In<sub>2</sub>O<sub>3</sub>/ZrO<sub>2</sub> for Highly Selective CO<sub>2</sub> Hydrogenation to Methanol. *J. Am. Chem. Soc.* **2020**, *142* (46), 19523–19531.
- (18) Chen, T.-Y.; Cao, C.; Chen, T.-B.; Ding, X.; Huang, H.; Shen, L.; Cao, X.; Zhu, M.; Xu, J.; Gao, J.; et al. Unraveling Highly Tunable Selectivity in CO<sub>2</sub> Hydrogenation over Bimetallic In-Zr Oxide Catalysts. *ACS Catal.* **2019**, *9* (9), 8785–8797.
- (19) Regalado Vera, C. Y.; Manavi, N.; Zhou, Z.; Wang, L.-C.; Diao, W.; Karakalos, S.; Liu, B.; Stowers, K. J.; Zhou, M.; Luo, H.; et al. Mechanistic understanding of support effect on the activity and selectivity of indium oxide catalysts for CO<sub>2</sub> hydrogenation. *Chemical Engineering Journal* **2021**, *426*, No. 131767.
- (20) Wei, Y.; Liu, F.; Ma, J.; Yang, C.; Wang, X.; Cao, J. Catalytic roles of In<sub>2</sub>O<sub>3</sub> in ZrO<sub>2</sub>-based binary oxides for CO<sub>2</sub> hydrogenation to methanol. *Molecular Catalysis* **2022**, *525*, No. 112354.
- (21) Ho, P. H.; Woo, J.-W.; Feizie Ilmasani, R.; Han, J.; Olsson, L. The role of Pd–Pt Interactions in the Oxidation and Sulfur Resistance of Bimetallic Pd–Pt/γ-Al<sub>2</sub>O<sub>3</sub> Diesel Oxidation Catalysts. *Ind. Eng. Chem. Res.* **2021**, *60* (18), 6596–6612.
- (22) Ghosh, S.; Sebastian, J.; Olsson, L.; Creaser, D. Experimental and kinetic modeling studies of methanol synthesis from CO<sub>2</sub> hydrogenation using In<sub>2</sub>O<sub>3</sub> catalyst. *Chemical Engineering Journal* **2021**, *416*, No. 129120.
- (23) Ho, P. H.; Jabłońska, M.; Palkovits, R.; Rodríguez-Castellón, E.; Ospitali, F.; Fornasari, G.; Vaccari, A.; Benito, P. N<sub>2</sub>O catalytic decomposition on electrodeposited Rh-based open-cell metallic foams. *Chemical Engineering Journal* **2020**, *379*, No. 122259.
- (24) Beller, M.; Renken, A.; Van Santen, R. *Catalysis From Principles to Applications*; Wiley-VCH, 2012.
- (25) Song, L.; Dou, K.; Wang, R.; Leng, P.; Luo, L.; Xi, Y.; Kaun, C.-C.; Han, N.; Wang, F.; Chen, Y. Sr-Doped Cubic In<sub>2</sub>O<sub>3</sub>/Rhombohedral In<sub>2</sub>O<sub>3</sub> Homo Junction Nanowires for Highly Sensitive and Selective Breath Ethanol Sensing: Experiment and DFT Simulation Studies. *ACS Appl. Mater. Interfaces* **2020**, *12* (1), 1270–1279.
- (26) Gao, L.; Ren, F.; Cheng, Z.; Zhang, Y.; Xiang, Q.; Xu, J. Porous corundum-type In<sub>2</sub>O<sub>3</sub> nanoflowers: controllable synthesis, enhanced ethanol-sensing properties and response mechanism. *CrystEngComm* **2015**, *17* (17), 3268–3276.
- (27) Zhu, H.; Wang, X.; Yang, F.; Yang, X. Template-Free, Surfactantless Route to Fabricate In(OH)<sub>3</sub> Monocrystalline Nanoarchitectures and Their Conversion to In<sub>2</sub>O<sub>3</sub>. *Cryst. Growth Des.* **2008**, *8* (3), 950–956.
- (28) Gan, J.; Lu, X.; Wu, J.; Xie, S.; Zhai, T.; Yu, M.; Zhang, Z.; Mao, Y.; Wang, S. C. I.; Shen, Y.; et al. Oxygen vacancies promoting photoelectrochemical performance of In<sub>2</sub>O<sub>3</sub> nanocubes. *Sci. Rep.* **2013**, *3* (1), 1021.
- (29) Frei, M. S.; Capdevila-Cortada, M.; García-Muelas, R.; Mondelli, C.; López, N.; Stewart, J. A.; Curulla Ferré, D.; Pérez-Ramírez, J. Mechanism and microkinetics of methanol synthesis via CO<sub>2</sub> hydrogenation on indium oxide. *J. Catal.* **2018**, *361*, 313–321.
- (30) Thommes, M.; Kaneko, K.; Neimark, A. V.; Olivier, J. P.; Rodriguez-Reinoso, F.; Rouquerol, J.; Sing, K. S. W. Physisorption of gases, with special reference to the evaluation of surface area and pore size distribution (IUPAC Technical Report). *Pure Appl. Chem.* **2015**, *87* (9–10), 1051–1069.
- (31) [https://srdata.nist.gov/xps/EngElmSrchQuery.aspx?EType=PE&CSOpt=Retri\\_ex\\_dat&Elm=In](https://srdata.nist.gov/xps/EngElmSrchQuery.aspx?EType=PE&CSOpt=Retri_ex_dat&Elm=In) (accessed October 2023).
- (32) <https://www.thermofisher.com/se/en/home/materials-science/learning-center/periodic-table/other-metal/indium.html> (accessed October 2023).
- (33) Sharma, P.; Hoang Ho, P.; Shao, J.; Creaser, D.; Olsson, L. Role of ZrO<sub>2</sub> and CeO<sub>2</sub> support on the In<sub>2</sub>O<sub>3</sub> catalyst activity for CO<sub>2</sub> hydrogenation. *Fuel* **2023**, *331*, No. 125878.
- (34) (a) Su, Y.-M.; Kuo, Y.-L.; Lin, C.-M.; Lee, S.-F. One-step fabrication of tetragonal ZrO<sub>2</sub> particles by atmospheric pressure plasma jet. *Powder Technol.* **2014**, *267*, 74–79. (b) Basahel, S. N.; Ali, T. T.; Mokhtar, M.; Narasimharao, K. Influence of crystal structure of nanosized ZrO<sub>2</sub> on photocatalytic degradation of methyl orange. *Nanoscale Res. Lett.* **2015**, *10* (1), 73.
- (35) Lackner, P.; Zou, Z.; Mayr, S.; Diebold, U.; Schmid, M. Using photoelectron spectroscopy to observe oxygen spillover to zirconia. *Phys. Chem. Chem. Phys.* **2019**, *21* (32), 17613–17620.
- (36) Sun, K.; Shen, C.; Zou, R.; Liu, C.-J. Highly active Pt/In<sub>2</sub>O<sub>3</sub>-ZrO<sub>2</sub> catalyst for CO<sub>2</sub> hydrogenation to methanol with enhanced CO

tolerance: The effects of ZrO<sub>2</sub>. *Applied Catalysis B: Environmental* **2023**, 320, No. 122018.

(37) Busca, G.; Lorenzelli, V. Infrared spectroscopic identification of species arising from reactive adsorption of carbon oxides on metal oxide surfaces. *Materials Chemistry* **1982**, 7 (1), 89–126.

(38) Reyes, L. M. *Surface Adsorption Studies of CO<sub>2</sub> and H<sub>2</sub> on Defected Indium Oxide: Insights into Gas-Phase Heterogeneous Photocatalysis*; University of Toronto, 2017; <https://tspace.library.utoronto.ca/handle/1807/97195> (accessed December 2023).

(39) Collins, S. E.; Baltanás, M. A.; Bonivardi, A. L. Infrared Spectroscopic Study of the Carbon Dioxide Adsorption on the Surface of Ga<sub>2</sub>O<sub>3</sub> Polymorphs. *J. Phys. Chem. B* **2006**, 110 (11), 5498–5507.

(40) Tsoukalou, A.; Serykh, A. I.; Willinger, E.; Kierzkowska, A.; Abdala, P. M.; Fedorov, A.; Müller, C. R. Hydrogen dissociation sites on indium-based ZrO<sub>2</sub>-supported catalysts for hydrogenation of CO<sub>2</sub> to methanol. *Catal. Today* **2022**, 387, 38–46.

(41) Yan, T.; Li, N.; Wang, L.; Ran, W.; Duchesne, P. N.; Wan, L.; Nguyen, N. T.; Wang, L.; Xia, M.; Ozin, G. A. Bismuth atom tailoring of indium oxide surface frustrated Lewis pairs boosts heterogeneous CO<sub>2</sub> photocatalytic hydrogenation. *Nat. Commun.* **2020**, 11 (1), 6095.

(42) Cárdenas-Arenas, A.; Quindimil, A.; Davó-Quñonero, A.; Bailón-García, E.; Lozano-Castelló, D.; De-La-Torre, U.; Pereda-Ayo, B.; González-Marcos, J. A.; González-Velasco, J. R.; Bueno-López, A. Isotopic and in situ DRIFTS study of the CO<sub>2</sub> methanation mechanism using Ni/CeO<sub>2</sub> and Ni/Al<sub>2</sub>O<sub>3</sub> catalysts. *Applied Catalysis B: Environmental* **2020**, 265, No. 118538.

(43) Yang, B.; Li, L.; Jia, Z.; Liu, X.; Zhang, C.; Guo, L. Comparative study of CO<sub>2</sub> hydrogenation to methanol on cubic bixbyite-type and rhombohedral corundum-type indium oxide. *Chin. Chem. Lett.* **2020**, 31 (10), 2627–2633.

(44) Numpilai, T.; Kidkhunthod, P.; Cheng, C. K.; Wattanakit, C.; Chareonpanich, M.; Limtrakul, J.; Witoon, T. CO<sub>2</sub> hydrogenation to methanol at high reaction temperatures over In<sub>2</sub>O<sub>3</sub>/ZrO<sub>2</sub> catalysts: Influence of calcination temperatures of ZrO<sub>2</sub> support. *Catal. Today* **2021**, 375, 298–306.

(45) (a) Dang, S.; Gao, P.; Liu, Z.; Chen, X.; Yang, C.; Wang, H.; Zhong, L.; Li, S.; Sun, Y. Role of zirconium in direct CO<sub>2</sub> hydrogenation to lower olefins on oxide/zeolite bifunctional catalysts. *J. Catal.* **2018**, 364, 382–393. (b) Dou, M.; Zhang, M.; Chen, Y.; Yu, Y. Theoretical study of methanol synthesis from CO<sub>2</sub> and CO hydrogenation on the surface of ZrO<sub>2</sub> supported In<sub>2</sub>O<sub>3</sub> catalyst. *Surf. Sci.* **2018**, 672–673, 7–12.

(46) Chen, P.; Tao, L.; Zhu, J.; Zhao, G.; Liu, Y.; Lu, Y. Morphology-Controllable Hexagonal-Phase Indium Oxide In Situ Structured onto a Thin-Felt Al<sub>2</sub>O<sub>3</sub>/Al-Fiber for the Hydrogenation of CO<sub>2</sub> to Methanol. *Energy Technol.* **2019**, 7 (3), No. 1800747.

(47) Chou, C.-Y.; Lobo, R. F. Direct conversion of CO<sub>2</sub> into methanol over promoted indium oxide-based catalysts. *Applied Catalysis A: General* **2019**, 583, No. 117144.